Impact on backpropagation of the spatial heterogeneity of sodium channel kinetics in the axon initial segment

Benjamin S.M. Barlow[a,*], André Longtin[a,b,c], and Béla Joós[a,b,*]

[a] *Department of Physics, University of Ottawa, STEM Complex, 150 Louis-Pasteur Pvt, Ottawa, ON, Canada, K1N 6N5*

[b] *Center for Neural Dynamics and AI, University of Ottawa, Ottawa, Canada*

[c] *Department of Cellular and Molecular Medicine, Faculty of Medicine, University of Ottawa, 451 Smyth Road, Ottawa, Ontario, Canada, K1H 8M5*

[*] *To whom correspondence should be addressed. E-mail: BenjaminSBarlow@icloud.com, BJoos@uOttawa.ca*

July 10, 2023

Keywords

- Axon Initial Segment
- Voltage-Gated Sodium Channel, $Na_V1.2$, $Na_V1.6$
- Backpropagation
- Pyramidal Neuron
- axonal stimulation
- somatic stimulation
- somatodendritic stimulation

1 Abstract

In a variety of neurons, action potentials (APs) initiate at the proximal axon, within a region called the axon initial segment (AIS), which has a high density of voltage-gated sodium channels (Na_Vs) on its membrane. In pyramidal neurons, the proximal AIS has been reported to exhibit a higher proportion of Na_Vs with gating properties that are "*right-shift*ed" to more depolarized voltages, compared to the distal AIS. Further, recent experiments have revealed that as neurons develop, the spatial distribution of Na_V subtypes along the AIS can change substantially, suggesting that neurons tune their excitability by modifying said distribution. When neurons are stimulated axonally, computational modelling has shown that this spatial separation of gating properties in the AIS enhances the backpropagation of APs into the dendrites. In contrast, in the more natural scenario of somatic stimulation, our simulations show that the same distribution impedes backpropagation. We implemented a range of hypothetical Na_V distributions in the AIS of a multicompartmental pyramidal cell model and investigated the precise kinetic mechanisms underlying such effects, as the spatial distribution of Na_V subtypes is varied. With axonal stimulation, proximal Na_V *availability* dominates, such that concentrating *right-shift*ed Na_Vs in the proximal AIS promotes backpropagation. However, with somatodendritic stimulation, the model is insensitive to *availability*. Instead, the higher *activation* threshold of *right-shift*ed Na_Vs in the AIS impedes backpropagation. Therefore, recently observed developmental changes to the spatial separation and relative proportions of $Na_V1.2$ and $Na_V1.6$ in the AIS differentially impact *activation* and *availability*. The effects on backpropagation, and potentially learning, are opposite for orthodromic versus antidromic stimulation.

2 Author Summary

Neurons use sodium ion currents, controlled by a neuron's voltage, to trigger signals called action potentials (APs). These APs typically result from synaptic input from other neurons onto the dendrites and soma. An AP is generated at the axon initial segment (AIS) just beyond the soma. From there, it travels down the axon to other cells, but can also propagate "backwards" towards the soma and dendrites. This "backpropagation" allows a comparison at synapses of the timing of outgoing and incoming signals, a feedback process that modifies synaptic connection strengths linked to learning. It is puzzling that in many neurons, sodium ion channels come in two types: high-voltage threshold channels clustered near the soma where the AIS begins, and low-voltage ones further away towards the axon. This separation changes in the early development of the animal, which raises the question of its role in backpropagation. We constructed a detailed mathematical model to explore how separation affects backpropagation. Separation either impedes or enhances learning, depending on whether the AP results from synaptic inputs or, less typically, currents moving backwards from the axon. This is explained by the different effects the separation has on two key kinetic processes that govern sodium currents.

3 Main text

3.1 Introduction

In fluorescence microscopy images of neurons, the axon initial segment (AIS) is visible as a patch of axonal membrane near the soma with a high density of voltage-gated ion channels. These channels enable the AIS to initiate and shape action potentials (spikes) and regulate neuronal excitability [1]. The AIS can be thought of as an organelle, that lives within the first $\approx 100\mu m$ of axonal membrane and whose function is to supply the current needed to initiate spikes when the neuron decides to fire —usually in response to synaptic input. The AIS can move, up and down the axon and also change its length on a timescale of hours to days. This phenomenon, called structural AIS plasticity, enables neurons to optimize their sensitivity to specific input frequencies during development and to homeostatically adjust their intrinsic excitability [2, 3, 4]. GABAergic input can also impinge on the AIS from axo-axonic synapses, such that the AIS can be modulated directly by interneurons. Synaptic input at the AIS can rapidly and precisely control the excitability of individual neurons for sound localization [5]. Fast AIS plasticity, including receptor-mediated changes to local ion channel properties and endocytosis of voltage-gated channels, occurs on timescales of seconds to minutes [6]. (This is distinct from pathological remodelling induced by ischemia, although in [7], it was recently demonstrated that cortical neurons are more robust to interruptions in blood flow than previously thought.) The outsized electrophysiological influence of the AIS demands robust characterization of this short piece of axon as it interacts with its environment.

Over three-quarters of all neurons in the mammalian cortex are pyramidal cells (see Figure S1), which have dendrites spanning the thickness of the cortex (several mm) and AIS lengths on the order of tens of μm [8, 9, 10]. The AIS requires a high density of voltage-gated sodium channels (Na_Vs) to prime and initiate action potentials [11, 12, 13]. In pyramidal cells, the AIS features two Na_V subtypes, with an interesting spatial distribution: $Na_V1.2$ channels cluster near the soma (i.e. at the proximal AIS) while $Na_V1.6$ cluster toward the distal AIS [14, 15, 16]. However, the purpose of this separated distribution of Na_V subtypes remains unclear [17, 18]. Further, recent experiments have revealed that as neurons develop, the spatial distribution of Na_Vs in the AIS can change substantially, suggesting that neurons tune their excitability by modifying said distribution [19].

It is a prevalent view that the Hodgkin-Huxley kinetics of $Na_V1.2$ are *right-shift*ed relative to those

of $Na_V1.6$ by an amount $V_{RS} \sim 10 - 15mV$ [20, 14]. The separated Na_V distribution is reported to promote backpropagation —which is important for learning— following axonal stimulation [14]. There is also evidence that mutations which alter the gating properties of $Na_V1.2$ are involved in epilepsy and autism [21]. Backpropagated spikes drive learning by depolarizing the postsynaptic membrane, which triggers metabolic events that give rise to synaptic plasticity, including spike-timing-dependent plasticity [22]. There is experimental evidence that postsynaptic backpropagation can release retrograde messengers into the synapse, and influence the future release of neurotransmitters from the presynaptic neuron [23]. APs can influence calcium spikes in dendrites [24]. And backpropagation can underlie bursting mechanisms in cortical neurons [25, 26], which makes it important for burst-dependent synaptic plasticity [27]. Other computational powers are attributed to the AIS. Moving the initiation site away from the soma (i.e. toward the distal AIS) beyond a critical distance enables high-frequency spiking in cortical neurons, increasing the maximum spike frequency by an order of magnitude [13]. Separating $Na_V1.6$ into the distal AIS is said to push the initiation site toward that location, owing to those channels' lower voltage threshold [14, 20]. However, in [28], simulations having only one Na_V type demonstrated that passive cable properties are sufficient to locate AP initiation at the distal AIS.

In our simulations, we alter the composition of the AIS and look for changes in the backpropagation threshold. The model neuron is allowed to distribute *right-shift*ed Na_V gating properties along the AIS, by differentially distributing two functionally distinct classes of sodium channels, referred to here as $Na_V1.2$ and $Na_V1.6$ following [14], [20] and [19]. Our modelling study is motivated by the following question: what effect does the separated spatial distribution of $Na_V1.2$ (or *right-shift*ed gating properties) and $Na_V1.6$ (*left-shift*) in the AIS have on excitability and backpropagation? In particular, how does the finding in [14], that the separated distribution of Na_V subtypes favours backpropagation, generalize to the more common situation of somatic stimulation? A natural approach is to systematically alter that Na_V distribution, by varying the extent to which Na_V subtypes are spatially segregated in the AIS without affecting the total Na_V density. We implement a variety of hypothetical Na_V density profiles in the AIS —presumably available to evolution— and compute the threshold for backpropagation in a biophysically detailed multicompartmental pyramidal cell. (Cell geometry is provided in Supplementary Information, Figure S1.) We show that Na_V separation enhances backpropagation with axonal stimulation but can impede it with somatic stimulation. This asymmetrical result was not expected.

To explain our results, we independently modify the *right-shift* (V_{RS}) of selected $\mathrm{Na_V1.2}$ gating variables and their respective time constants by an amount ΔV_{RS} (i.e. $V_{\mathrm{RS}} \longrightarrow V_{\mathrm{RS}} + \Delta V_{\mathrm{RS}}$). These modifications to $\mathrm{Na_V1.2}$ gating are applied only in the AIS. Sweeping ΔV_{RS} (while clamping other gating variables to nominal V_{RS} values) reveals that (I) $\mathrm{Na_V1.2}$ *availability* and its time constant explain how proximal $\mathrm{Na_V1.2}$ promotes backpropagation with axonal stimulation, and (II) the threshold of steady-state *activation* explains how $\mathrm{Na_V1.2}$ suppresses backpropagation and reduces excitability with somatic stimulation.

3.2 Results

3.2.1 Hypothetical $\mathrm{Na_V}$ distributions in the AIS

The standard AIS length in our model is $25\ \mu m$, based on measurements from [10]. A key feature of the $\mathrm{Na_V}$ distribution that changes during development, is the extent to which the voltage-gated sodium channel subtypes $\mathrm{Na_V1.2}$ and $\mathrm{Na_V1.6}$ are localized in the proximal and distal AIS, respectively. In these simulations, the relative proportion of $\mathrm{Na_V1.2}$ versus $\mathrm{Na_V1.6}$ at a given position along the AIS can be changed without affecting the total $\mathrm{Na_V}$ density at any point (Equation 3). Figure 1 shows how the parameters x and κ control the way $\mathrm{Na_V}$ subtypes are spread out along the AIS. When x is at its highest value of 1, the subtypes $\mathrm{Na_V1.2}$ and $\mathrm{Na_V1.6}$ are spaced apart from each other, with $\mathrm{Na_V1.2}$ concentrated in the proximal AIS and $\mathrm{Na_V1.6}$ in the distal AIS. Decreasing x transforms this separated distribution into a uniform mix ($x = 0$) where $\mathrm{Na_V1.2}$ and $\mathrm{Na_V1.6}$ are distributed homogeneously. This can be seen in Figure 1a. Every distribution except the uniform $\mathrm{Na_V}$ mix has a location along the AIS at which the density of $\mathrm{Na_V1.6}$ overtakes the $\mathrm{Na_V1.2}$ density. That location, which we call the $\mathrm{Na_V}$ crossover and denote κ, is also varied in our simulations as can be seen in Figure 1b (κ is a dimensionless length normalized by the AIS length). To cement our results, we will further apply identical transformations to the $\mathrm{Na_V}$ distribution in a cell having a 'backward' AIS, that is, with *distal* $\mathrm{Na_V1.2}$ and *proximal* $\mathrm{Na_V1.6}$. The results from the backward AIS model are nearly a mirror image of our findings.

For each hypothetical $\mathrm{Na_V}$ distribution, a short current pulse ($1ms$) is injected at a specific site, and the minimum (i.e. threshold) pulse amplitude I (in nA) required to elicit a spike is determined. Brief pulse durations separate the stimulation waveform from the intrinsic response of the cell. We define excitability in terms of two thresholds: backpropagation threshold I_{BP} (AP leading to a spike in the distal

dendrites) and forward-propagation threshold I_{FP} (axonal AP with or without backpropagation). Current is injected either in the middle of the soma (somatic stimulation) or the axon just distal to the AIS (axonal stimulation). Both are used by experimentalists [29], and certain pyramidal neurons are also known to receive axo-axonic input at the AIS as well as somatodendritic input [6]. In both cases, forward propagation refers to an AP travelling down the axon, and backpropagation always refers to an AP visible as a spike in the dendrites. Backpropagation was deemed to have occurred when the mean peak voltage of dendritic tips exceeded $-10.0mV$ following stimulation (see Supplementary Information, Figure S2).

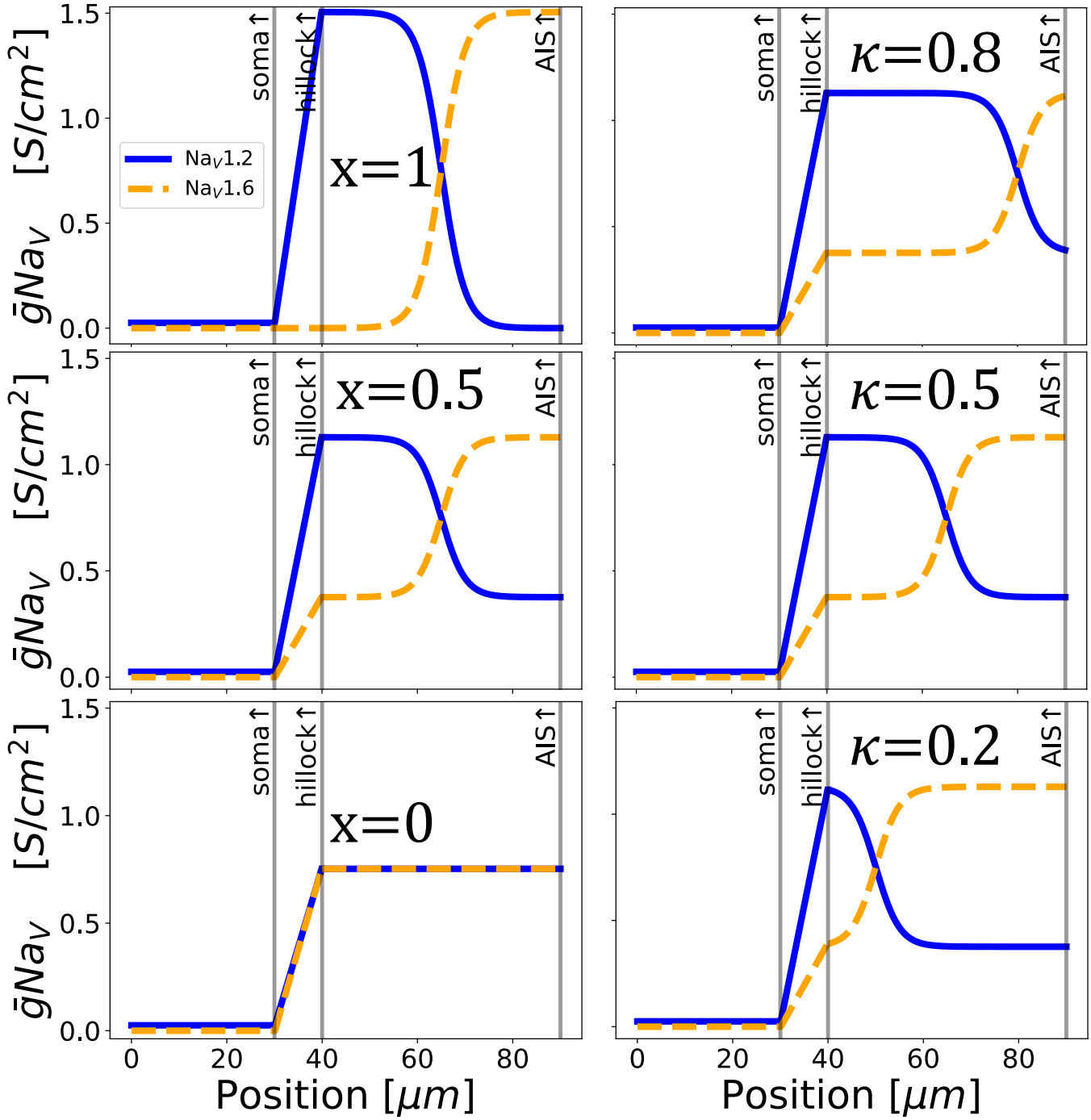

(a) (b)

Figure 1: Modifying the spatial distribution of Na_V subtypes in the AIS while keeping the total conductance constant. (a) The spatial separation of Na_V subtypes in the AIS is varied using the parameter "x" with $\kappa = 0.5$. The top plot is a model setup with a separated distribution [14] of Na_Vs in the AIS. The high threshold $Na_V1.2$ (indicated in blue) are concentrated close to the soma, and the low threshold $Na_V1.6$ (indicated in orange) are kept distal to the soma. Moving from top to bottom, both Na_V subtypes are distributed ever more evenly along the AIS. We chose the parameter name "x" to vary the spatial separation of the AIS Na_V distributions, because the separated distribution is x-shaped. Setting $x = 1$ in our simulations gives the separated distribution, and $x = 0$ gives the "flat" distribution wherein both Na_V subtypes are uniformly mixed. (b) Variation of the crossover location (κ) of Na_Vs in the AIS with $x = 0.5$. We have lengthened the AIS to $50\mu m$ in this graphic for visual clarity.

3.2.2 Somatic stimulation

In Figure 2, both negatively and positively sloped backpropagation threshold curves with respect to x are present, indicating that Na_V separation can promote or impede backpropagation (respectively). Changes in threshold can be as large as 30%. Moving the Na_V crossover (κ) toward the distal AIS shifts the backpropagation threshold curves upward. A qualitative change, namely the sign of the slope, occurs around $\kappa = 0.4$.

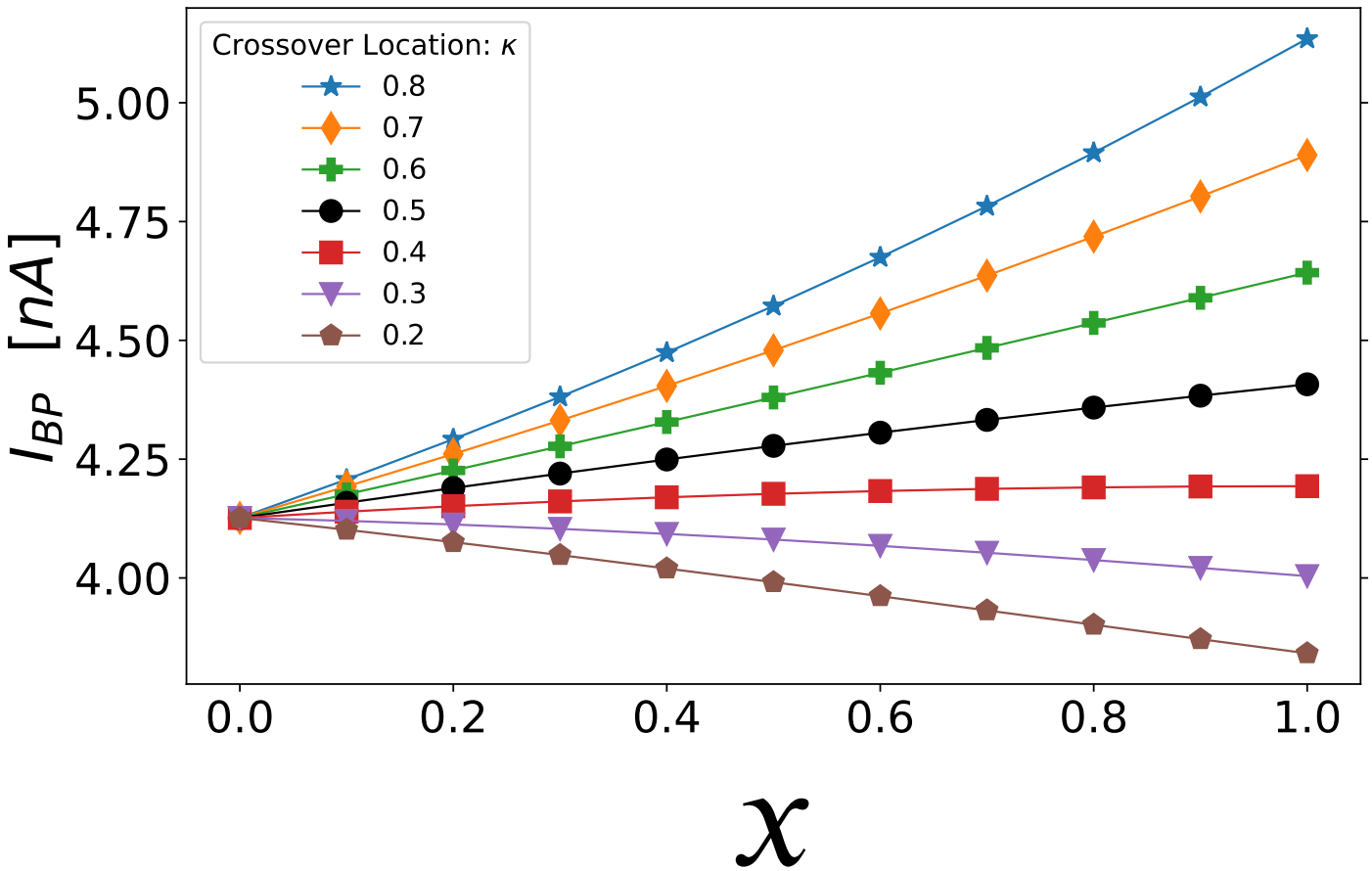

Figure 2: Somatic Stimulation: Combined effect of varying crossover location (κ) and Na_V separation (x) in the axon initial segment. The threshold for forward AP propagation is the same as for backpropagation. Varying the separation parameter "x" from $x = 0$ to $x = 1$, the distribution of Na_V channels goes from flat (homogeneous) to separated, the latter approximating the distribution observed in developing pyramidal neurons (see Figure 1a). Note that curves for all values of κ converge to a single point at $x = 0$ since κ can have no effect when the two Na_V's are uniformly distributed along the AIS. The lines have been drawn to guide the eye.

An intuitive explanation for this latter effect is that moving the crossover location away from the soma causes the AIS to be dominated by $Na_V1.2$ channels (see Figure 1b, $\kappa = 0.8$), which have a higher voltage

threshold than $Na_V1.6$. APs still initiate in the distal AIS, but the dominant $Na_V1.2$ renders the cell less excitable. Further, for $\kappa \gtrsim 0.4$, the backpropagation threshold increases as we tend toward the separated, x-shaped distribution of Na_Vs. This behaviour is the opposite of what is observed for axonal stimulation below and in [14]. We repeated these simulations with AIS length up to $100\mu m$ (Figure S3) and also with stimulation at the main apical dendrite (Figure S5) instead of the soma, and obtained the same qualitative results as Figure 2 (see Supplementary Information Section S1.3).

The negatively sloped curves do not necessarily imply that proximal $Na_V1.2$ promotes backpropagation in the case of somatic stimulation. In those curves ($\kappa \lesssim 0.4$), the AIS is mainly populated with $Na_V1.6$ when $x > 0$. Also note that decreasing κ places more $Na_V1.6$ channels nearer to the soma (see Figure 1b, $\kappa = 0.2$). In that case, the threshold-lowering effect of Na_V separation could come from the increased total $Na_V1.6$ density that results from increasing x when κ is relatively small, rather than from the proximal accumulation of $Na_V1.2$ with increasing x. Further, increasing κ (which increases the ratio of $Na_V1.2$ to $Na_V1.6$ in the AIS) raises the threshold for all curves in Figure 2 (see also Figure S4). It is then consistent to postulate that for somatic stimulation, the backpropagation threshold is increased by AIS $Na_V1.2$ at all values of x and κ, and Figure 2 is consistent with AIS $Na_V1.6$ enhancing excitability and backpropagation. In other words, for **somatic stimulation**:

- when $\kappa < 0.5$ and $x > 0$, the AIS is dominated by $Na_V1.6$: increasing x increases the proportion of total AIS Na_V conductance due to $Na_V1.6$ (negative slope: separated distribution yields the lowest backpropagation threshold).

- when $\kappa > 0.5$ and $x > 0$, the AIS is dominated by $Na_V1.2$: increasing x decreases the proportion of total AIS Na_V conductance due to $Na_V1.6$ (positive slope: separated distribution yields the highest backpropagation threshold).

Lengthening the hillock with κ fixed also moves the crossover away from the soma. Curves with negative slope in Figure 2 became positively sloped when the hillock was lengthened from $10\mu m$ to $30\mu m$ (Figure S6). The forward propagation threshold for somatic stimulation with a single $1ms$ current pulse is not included in a separate figure since it is identical to the backpropagation threshold in this model. This does not depend on the somatic injection site.

An informative variation on Figure 2 is shown in Figure 3c in which the AIS is "put on backward",

such that $Na_V1.2$ is concentrated in the distal AIS and $Na_V1.6$ is proximal to the soma. As one might expect, the effect of varying χ and κ in Figure 3 is opposite to what is seen in Figure 2, albeit with some new curvature at low κ. This reinforces the observation that proximal $Na_V1.6$ facilitates backpropagation with somatic stimulation.

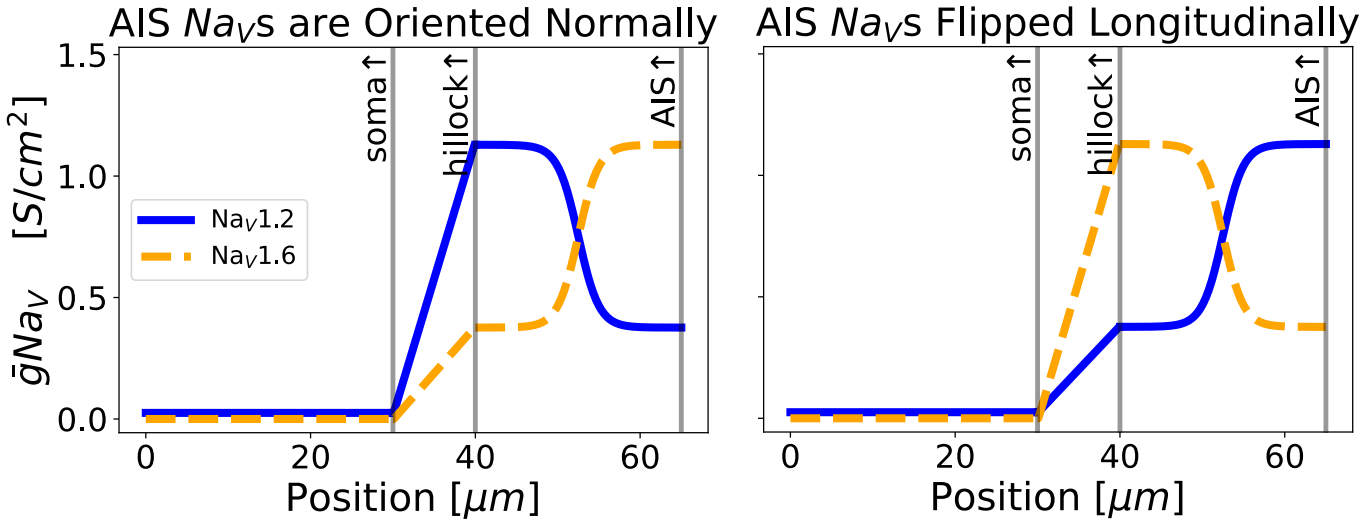

(a) (b)

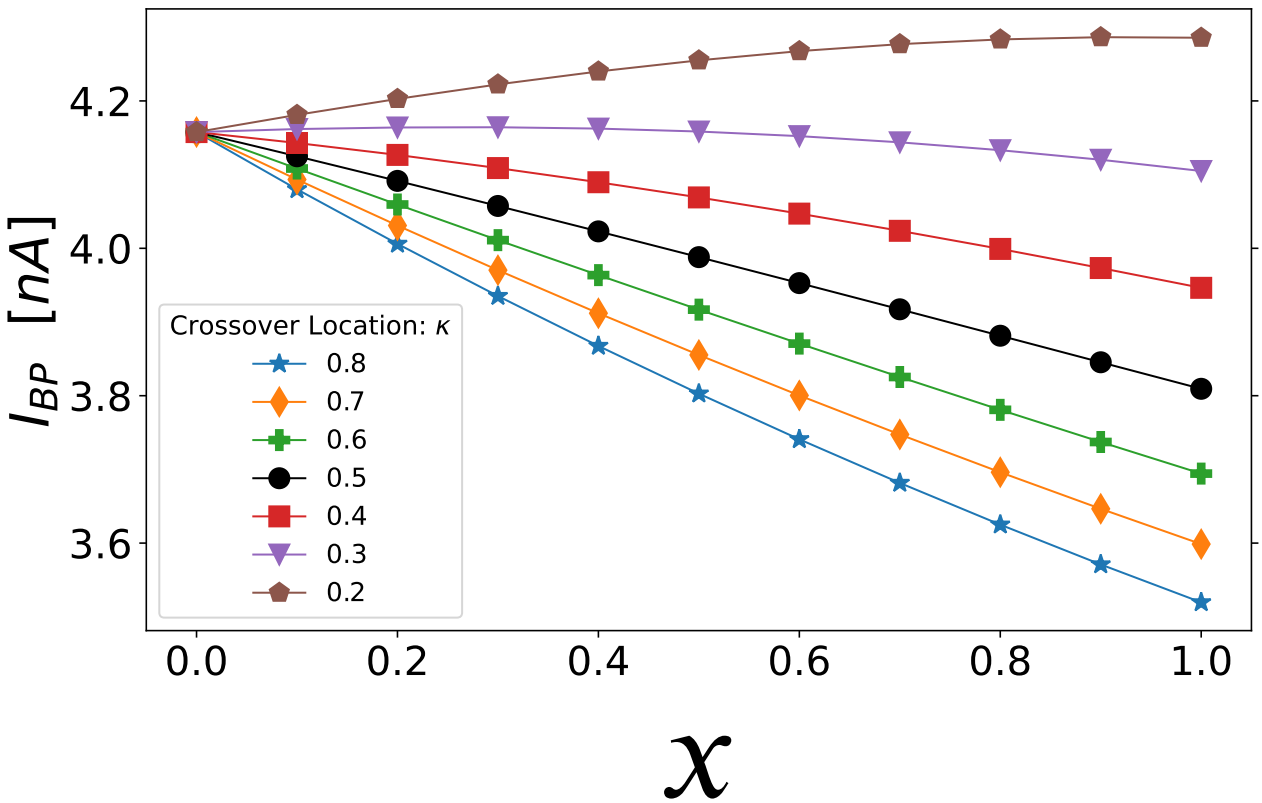

(c)

Figure 3: When the AIS Na_V distribution is flipped, setting $x = 1$ concentrates $Na_V1.6$ at the proximal AIS and $Na_V1.2$ at the distal AIS —the opposite of what is observed in many pyramidal cells [14, 15, 16]. (a) AIS with proper longitudinal placement of Na_Vs. (b) AIS with a longitudinally flipped Na_V distribution. In both plots, $x = 0.5$ and $\kappa = 0.5$. (c) Somatic stimulation with AIS Na_Vs flipped as in (b): This result is close to a mirror image of Figure 2. The lines have been drawn to guide the eye.

3.2.3 Axonal stimulation

With axonal stimulation (current injection just distal to the AIS), Na_V separation consistently lowers the backpropagation threshold (Figure 4). Contrary to somatic stimulation (Figure 2), moving the Na_V crossover (κ) toward the distal AIS shifts the backpropagation threshold curves downward.

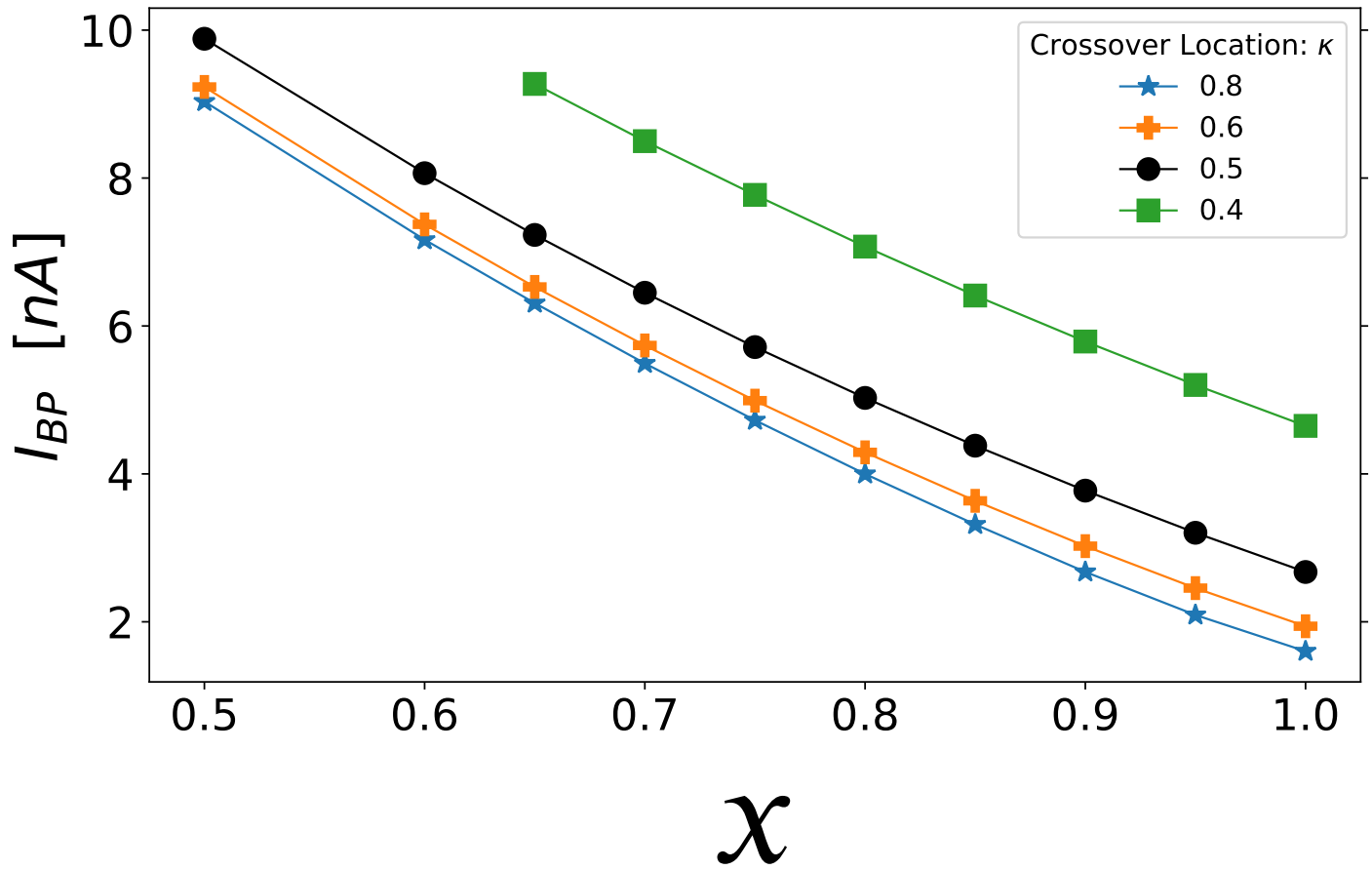

Figure 4: Axonal Stimulation: Effect of varying crossover location (κ) and Na_V separation (x) in the AIS on the backpropagation threshold (see Figure 1). When computing the threshold, the stimulating current was limited to a maximum of $10nA$, to prevent unphysiological local depolarization at the stimulation site. Due to the smaller diameter of the axon (relative to the soma), $10nA$ is sufficient to depolarize the membrane potential to $\approx +80mV$ at the stimulation site, whereas the resting potential is $V_{\text{rest}} = -70mV$. To achieve backpropagation within that constraint (following axonal stimulation), our model required some amount of proximal $Na_V1.2$, delivered through the combined effects of Na_V separation ($x \gtrsim 0.5$) and a sufficiently distal crossover position $\kappa \gtrsim 0.4$. Separating the two Na_V subtypes ($x \longrightarrow 1$) lowers the threshold, in agreement with the finding in [14] that proximal accumulation of $Na_V1.2$ promotes backpropagation, albeit due to different gating properties (Figure 6a). Increasing κ raises the proportion of $Na_V1.2$ (relative to $Na_V1.6$) in the AIS and lowers the backpropagation threshold as well. Threshold changes here are larger than for somatic stimulation (Figure 2). The lines have been drawn to guide the eye.

The decreasing threshold with respect to x in Figure 4 is consistent with the conclusion from [14], which

used axonal stimulation, that proximal $Na_V1.2$ in the AIS promotes backpropagation. Our results for κ, with axonal stimulation, provide new support for their findings. This agreement is interesting because our method of modifying the AIS Na_V distribution (described above in Figure 1) is quite different from their simulations which scaled the density of $Na_V1.2$ by a constant, leaving the $Na_V1.6$ profile intact. We expect such scaling to have the same effect in our model since increasing or decreasing the density of $Na_V1.2$ in a separated distribution with a specified κ and $x > 0$ would scale the total AIS Na_V conductance, especially at the proximal AIS.

The forward-propagation threshold I_{FP}, also referred to as the AP threshold, is shown in Figure 5. Stimulation amplitude is an order of magnitude lower than in the case of the backpropagation threshold. This is expected with axonal stimulation due to the high Na_V density of the distal AIS, its electrical isolation from the soma, and its proximity to the stimulus. Na_V separation concentrates $Na_V1.6$ in the distal AIS, making it more excitable in the portion nearer to the stimulation site. This finding is consistent with [14], who found that distal $Na_V1.6$ density places the lowest initiation threshold (and therefore the AP trigger zone) at the distal AIS. However, [28] has shown that cable properties are sufficient to explain why the trigger zone is located at the distal AIS (see Discussion). Moving the crossover distally ($\kappa \longrightarrow 1$) increases the total proportion of $Na_V1.2$ in the AIS and thereby raises the I_{FP} threshold due to *activation* right-shift.

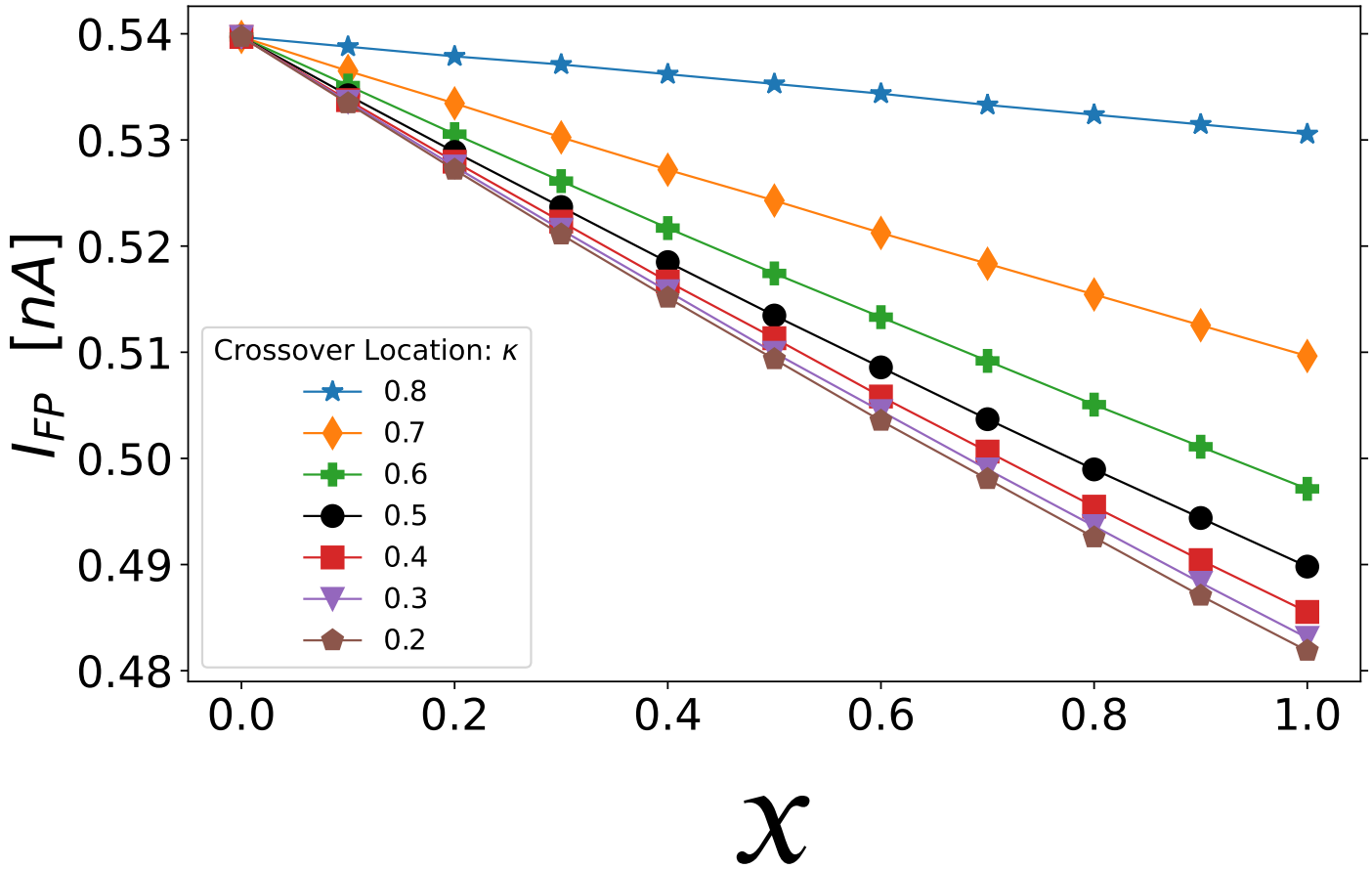

Figure 5: Axonal Stimulation: Effect of x and κ on forward propagation threshold. The trend for all constant κ curves is that raising the proportion of total AIS $Na_V1.6$ (by reducing κ) or concentrating $Na_V1.6$ in the distal AIS (by increasing x) lowers the threshold to initiate forward propagating action potentials (see Figure 1). Note that this threshold current pulse is not sufficient to achieve backpropagation. The effect of Na_V separation is much smaller here than for the backpropagation threshold. The lines have been drawn to guide the eye.

3.2.4 Modifying the *right-shift* of selected gating properties in the AIS

Na_V subtypes are defined by their gating properties. Each Na_V distribution (Figure 1) produces a corresponding spatial profile of gating properties, including *right-shift*. In Figure 6, we unravel the effects of Na_V separation on the backpropagation threshold in terms of the resulting spatial distribution of Na_V *right-shift* associated with $Na_V1.2$. Gating properties are detailed in Supplementary Information, see Figure S7.

Our model sets the nominal *right-shift* of $Na_V1.2$ at $V_{RS} = 13.0mV$ for compatibility with [14]. In Figure 6, the AIS Na_V distribution is fixed at $x = 1$. This spatial separation of Na_Vs concentrates *right-shift* in the proximal AIS by concentrating $Na_V1.2$ in that region (see Figure 1). We use the parameter ΔV_{RS} to alter, in the AIS only, the *right-shift* of specific $Na_V1.2$ gating properties; $\Delta V_{RS} = 0$ for the nominal

$\mathrm{Na_V1.2}$ properties.

The *activation* $m^{\mathrm{Na_V1.2}}$ and *availability* $h^{\mathrm{Na_V1.2}}$ of real $\mathrm{Na_V1.2}$ channels in nature are *right-shift*ed by similar amounts relative to their $\mathrm{Na_V1.6}$ counterparts [20, 14, 12, 30]. (Although certain receptors can temporarily *right-shift activation* without shifting steady-state *availability* [31].) In our simulations, simultaneously altering the *right-shift* of $m^{\mathrm{Na_V1.2}}$ and $h^{\mathrm{Na_V1.2}}$ produces the 'reference curves' legended '●' in Figure 6a and Figure 6b. In the reference curves, ΔV_{RS} shifts the voltage-dependence of every $\mathrm{Na_V1.2}$ gating property. That is, as functions of membrane potential, the steady-states and time constants are $m_\infty^{\mathrm{Na_V1.2}} = m_\infty^{\mathrm{Na_V1.2}}(V - \Delta V_{\mathrm{RS}})$, $\tau_m^{\mathrm{Na_V1.2}} = \tau_m^{\mathrm{Na_V1.2}}(V - \Delta V_{\mathrm{RS}})$, $h_\infty^{\mathrm{Na_V1.2}} = h_\infty^{\mathrm{Na_V1.2}}(V - \Delta V_{\mathrm{RS}})$, $\tau_h^{\mathrm{Na_V1.2}} = \tau_h^{\mathrm{Na_V1.2}}(V - \Delta V_{\mathrm{RS}})$ in the AIS.

Figure 6 connects gating properties to the results in Figure 4 and Figure 2. The reference curves confirm that proximal *right-shift* from $\mathrm{Na_V1.2}$ lowers the backpropagation threshold for axonal stimulation (Figure 6a) and *right-shift* raises I_{BP} for somatic stimulation (Figure 6b). Since ΔV_{RS} only affects the $\mathrm{Na_V1.2}$ channels within the AIS, we have demonstrated that *right-shift*ed gating properties within the AIS alone are sufficient to explain the effects of $\mathrm{Na_V}$ distribution on the backpropagation threshold shown above.

Further in Figure 6, we "shift-clamp" selected gating properties: Ignoring the experimental fact that $\mathrm{Na_V}$ *activation* and *availability* tend to *right-shift* in unison [20, 30, 32, 33] and that gating variables and their voltage-sensitive time constants *right-shift* together as well [34], we isolate the effects of individual gating properties by

1. applying ΔV_{RS} to $h^{\mathrm{Na_V1.2}}$ independently of $m^{\mathrm{Na_V1.2}}$,
2. applying ΔV_{RS} to $\tau_h^{\mathrm{Na_V1.2}}(V)$ independently of $h_\infty^{\mathrm{Na_V1.2}}(V)$, and likewise for $\tau_m^{\mathrm{Na_V1.2}}$, $m_\infty^{\mathrm{Na_V1.2}}$;

and compute the new backpropagation threshold $I_{BP}(\Delta V_{\mathrm{RS}})$. (For mathematical details, see Section 3.4.3.) An example of the latter is Equation 1 below, in which only $\tau_h^{\mathrm{Na_V1.2}}$ has its *right-shift* modified by ΔV_{RS}. The other three $\mathrm{Na_V1.2}$ variables have the nominal *right-shift* of $13mV$. The $I_{BP}(\Delta V_{\mathrm{RS}})$ curves in Figure 6

that correspond to Equation 1 are legended ■ $\tau_h^{\mathrm{Na_V1.2}}$:

$$\text{“}\blacksquare\,\tau_h^{\mathrm{Na_V1.2}}\text{”} \longleftarrow \begin{cases} \tau_h^{\mathrm{Na_V1.2}} = \tau_h^{\mathrm{Na_V1.2}}(V - \Delta V_{\mathrm{RS}}) \\ h_\infty^{\mathrm{Na_V1.2}} = h_\infty^{\mathrm{Na_V1.2}}(V) \\ \tau_m^{\mathrm{Na_V1.2}} = \tau_m^{\mathrm{Na_V1.2}}(V) \\ m_\infty^{\mathrm{Na_V1.2}} = m_\infty^{\mathrm{Na_V1.2}}(V). \end{cases} \tag{1}$$

(Figure S8 visualizes the impact of Equation 1 on gating properties as a function of position at V_{rest}.)

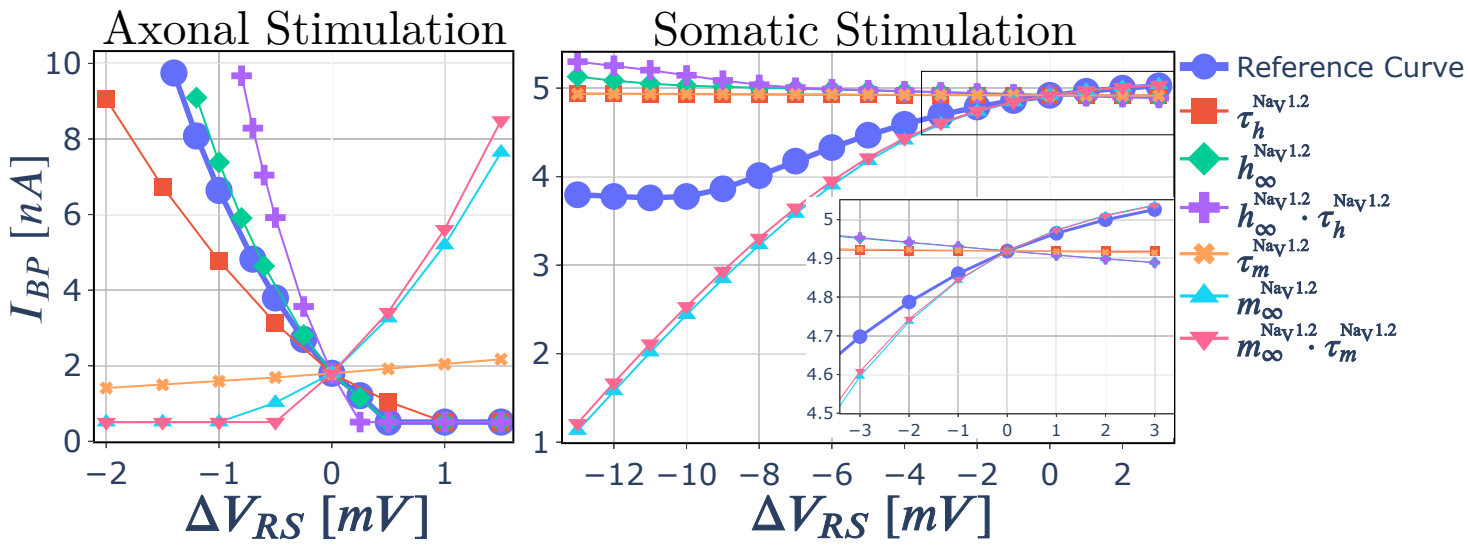

(a) (b)

Figure 6: Shift-Clamping selected gating properties reveals competing effects of $\mathrm{Na_V1.2}$ *right-shift* on the backpropagation threshold. In the AIS, ΔV_{RS} modifies the *right-shift* of $\mathrm{Na_V1.2}$ gating properties indicated in the legend. The slope of the reference curve (legended ●) shows the net effect of *right-shift* on I_{BP}. Points on this curve are pulled toward all of the other shift-clamped curves, but to varying degrees. Comparing each curve to its respective reference curve reveals the key gating properties through which *right-shift* controls backpropagation for each type of stimulation. **(a) Axonal stimulation:** The reference curve has a negative slope (*right-shift* lowers I_{BP}), and tracks curves legended with $h_\infty^{\mathrm{Na_V1.2}}$ or $\tau_h^{\mathrm{Na_V1.2}}$. The backpropagation threshold is governed by proximal $\mathrm{Na_V}$ *availability*, owing to the *right-shift* of $\mathrm{Na_V1.2}$, and is sensitive to the *right-shift* of its time constant. **(b) Somatic stimulation:** The reference curve has a positive slope near the nominal point (*right-shift* raises I_{BP}), and tracks curves legended with $m_\infty^{\mathrm{Na_V1.2}}$ near the nominal value of V_{RS} ($\Delta V_{\mathrm{RS}} \longrightarrow 0$, see inset). The backpropagation threshold is governed by $\mathrm{Na_V}$ steady-state *activation* and is insensitive to the *right-shift* of all $\mathrm{Na_V}$ time constants. The lines have been drawn to guide the eye. In both plots, $x = 1.0$ and $\kappa = 0.7$. Results are summarized in Table 1.

To unpack Figure 6 we start at the 'nominal point', which is the backpropagation threshold at $\Delta V_{\mathrm{RS}} = 0$,

for axonal stimulation in Figure 6a and for somatic stimulation in Figure 6b. All curves in Figure 6a and Figure 6b intersect at their respective nominal point because $\mathrm{Na_V1.2}$ *right-shift* is nominal there for all gating properties. Starting at the nominal point, as one moves leftward along a given curve ($\Delta V_{\mathrm{RS}} < 0$), *right-shift* is removed from the gating properties indicated in the legend only.

Figure 6a reveals that with axonal stimulation, the *right-shift* of *availability* drives I_{BP}. The *right-shift*ed steady-state *availability* $h_\infty^{\mathrm{Na_V1.2}}$ and voltage-dependent time constant of *availability* $\tau_h^{\mathrm{Na_V1.2}}$ work together to promote backpropagation (curve legended ✚ $h_\infty^{\mathrm{Na_V1.2}} \cdot \tau_h^{\mathrm{Na_V1.2}}$), overpowering the threshold-raising influence of *activation right-shift* (▼ $m_\infty^{\mathrm{Na_V1.2}} \cdot \tau_m^{\mathrm{Na_V1.2}}$). Further, removing the *right-shift* of $\tau_h^{\mathrm{Na_V1.2}}$ stops backpropagation: in the ■ $\tau_h^{\mathrm{Na_V1.2}}$ curve, all other gating properties, including $h_\infty^{\mathrm{Na_V1.2}}$, retain their nominal *right-shift*, yet backpropagation ceases when $\Delta V_{\mathrm{RS}} \lesssim -2mV$.

For somatic stimulation (Figure 6b) the *right-shift* of *activation* drives I_{BP}. The most significant decrease in threshold occurs in the ▲ $m_\infty^{\mathrm{Na_V1.2}}$ and ▼ $m_\infty^{\mathrm{Na_V1.2}} \cdot \tau_m^{\mathrm{Na_V1.2}}$ curves as the nominal *right-shift* is removed ($\Delta V_{\mathrm{RS}} \longrightarrow -13.0mV$). The ▼ $m_\infty^{\mathrm{Na_V1.2}} \cdot \tau_m^{\mathrm{Na_V1.2}}$ curve differs negligibly from the ▲ $m_\infty^{\mathrm{Na_V1.2}}$ curve, showing that $m_\infty^{\mathrm{Na_V1.2}}$ *right-shift* dominates in raising the threshold near the nominal point, and the *right-shift* of $\tau_m^{\mathrm{Na_V1.2}}$ matters little. Our ΔV_{RS} results are summarized in Table 1.

Table 1: Summary of Figure 6: Impact of *right-shift*ed $\mathrm{Na_V1.2}$ gating properties in the AIS on backpropagation threshold, revealed via shift-clamping.

Type of Stimulation	● reference curve	Increasing ΔV_{RS} of ***availability***		
		■ $\tau_h^{\mathrm{Na_V1.2}}$	◆ $h_\infty^{\mathrm{Na_V1.2}}$	✚ $h_\infty^{\mathrm{Na_V1.2}} \cdot \tau_h^{\mathrm{Na_V1.2}}$
Axonal	↓	↓	↓	↓
Somatic	↑	×	↓(slight)	↓(slight)
		Increasing ΔV_{RS} of ***activation***		
		✖ $\tau_m^{\mathrm{Na_V1.2}}$	▲ $m_\infty^{\mathrm{Na_V1.2}}$	▼ $m_\infty^{\mathrm{Na_V1.2}} \cdot \tau_m^{\mathrm{Na_V1.2}}$
Axonal	↓	↑ (slight)	↑	↑
Somatic	↑	×	↑	↑

Arrows (↓,↑) indicate the sign of the **slopes** of backpropagation threshold curves in Figure 6a (axonal stimulation) and Figure 6b (somatic stimulation). A downward arrow (↓) indicates that the backpropagation threshold I_{BP} decreases with increasing *right-shift*, applied to the kinetic variable(s) specified above it. Likewise, an upward arrow (↑) indicates an increased threshold when that combination of $\mathrm{Na_V1.2}$ variables is *right-shift*ed. In cells marked "×" the effect of *right-shift* was negligible.

3.3 Discussion

In early development, pyramidal neurons concentrate $Na_V1.2$ in the proximal AIS, and $Na_V1.6$ in the distal AIS. As these cells mature, $Na_V1.6$ invades the proximal AIS, and the two Na_V subtypes lose their separated distribution [19]. We have proposed a model for investigating the effects of Na_V separation in the axon initial segment on the initiation and backpropagation of action potentials. Our modelling indicates that the effects of the separated Na_V distribution depend on whether stimulation is orthodromic (e.g. somatodendritic input) or antidromic (e.g. axonal stimulation).

With somatic stimulation, the greater the proportion of $Na_V1.2$ in the AIS, relative to $Na_V1.6$, the less excitable the cell becomes. This is contrary to past modelling which used axonal current injection [14], though it is consistent with the experimental results in [17] where somatic stimulation was used. The threshold-raising effect of proximal $Na_V1.2$ is confirmed by repeating the simulations with a model cell in which the AIS has been flipped longitudinally (Figure 3), placing $Na_V1.6$ proximally and $Na_V1.2$ distally in the AIS.

Our results for axonal stimulation agree qualitatively with and expand upon past modelling efforts [14]. Excitability is greatest when Na_V subtypes are separated in the AIS. We show that both Na_V separation 'x-distribution' and distal translation of the crossover location κ promote backpropagation. That is, proximal accumulation of $Na_V1.2$ lowers the threshold for backpropagation. Further, increasing the total proportion of $Na_V1.2$ in the AIS —by moving the Na_V crossover distally— promotes backpropagation as well. We also find that increased distal $Na_V1.6$ concentration (which results from the separated distribution) lowers the AP threshold (Figure 5).

Testing both modes of stimulation can contribute to resolving inconsistencies between experiments such as [17] and [14], where stimulation was orthodromic in the former and antidromic in the latter. In [17], AP initiation was observed in pyramidal neurons which were engineered to be $Na_V1.6$-deficient. In those neurons, the AIS was populated entirely with $Na_V1.2$, however they still found that the AIS Na_V current was *left-shift*ed relative to the somatic current. From this and other observations, the authors in [17] suggest that the distribution of Na_V subtypes is not so important in shifting the local voltage-gated Na^+ current. We note that, compared to control neurons, the $Na_V1.6$-deficient neurons' AIS Na_V current was *right-shift*ed, and the orthodromic AP threshold (amplitude of a $2ms$ current pulse) was nearly doubled. This is consistent with our results and the modelling assumption that *right-shift* is associated with $Na_V1.2$

in the AIS —the model is agnostic about the molecular details. The decrease in excitability reported in [17] may have been even larger had they used more mature neurons. Their neurons were obtained from 4-5 week old mice, at which point the AIS will still be largely populated with $Na_V1.2$, whereas in wild type mice $Na_V1.6$ replaces much of the $Na_V1.2$ by 90 days [19, 24]. Our results indicate that with axonal stimulation, $Na_V1.6$-deficient cells may have a lower backpropagation threshold than the wild type.

The loss of the separated Na_V distribution in the AIS at later developmental stages, accompanied by the proximal localization of $Na_V1.6$, may enhance excitability to healthy orthodromic stimulation while protecting against the backpropagation of ectopic activity from damaged axons into the soma and dendrites. Further, research into the genetic causes of autism spectrum disorder has revealed that $Na_V1.2$ knockout can enhance pyramidal cells' tendency to send action potentials and simultaneously reduce backpropagation (somatodendritic hypoexcitability) [18]. Whereas [18] reported an interplay between $Na_V1.2$ and K_V, in contrast, our results are explained by the spatial distribution of Na_V *right-shift* within the AIS (Table 1, Figure 6b). Indeed, the reduced excitability resulting from AIS $Na_V1.2$ owes to the asymmetric impact of AIS Na_V *availability* on backpropagation in axonal versus somatic stimulation.

Although *right-shift*ing $Na_V1.2$ steady-state *availability* $h_\infty^{Na_V1.2}(V)$ in the AIS is necessary to promote backpropagation when stimulation is axonal, it is not sufficient on its own: our modelling shows that the voltage-sensitive time constant $\tau_h^{Na_V1.2}(V)$ must be *right-shift*ed as well (Figure 6a). *Right-shift*ing steady-state $Na_V1.2$ *availability alone* (◆$h_\infty^{Na_V1.2}$) increases Na^+ conductance at all voltages, as $h_\infty^{Na_V1.2}(V)$ is monotonically decreasing. It is clear then why ΔV_{RS} lowers the threshold in the ◆$h_\infty^{Na_V1.2}$ curves of Figure 6a and Figure 6b. However, it was not obvious that removing the nominal *right-shift* of voltage-sensitive time constants, without modifying steady-state *activation* or *availability*, should on its own be sufficient to eliminate the backpropagation threshold-lowering effects of $Na_V1.2$ for axonal stimulation. But that is what our model has demonstrated in the curve legended ■$\tau_h^{Na_V1.2}$ in Figure 6a. It follows that the x-distribution's tendency to promote backpropagation is not merely a result of increased steady-state *availability* of proximal AIS Na_Vs, but is a dynamic effect —dependent on the *right-shift* of $\tau_h^{Na_V1.2}(V)$ as well.

There is an interplay between cable properties and the distribution of Na_Vs in determining the site of AP initiation [35]. Electrical isolation of the initiation site may amplify the effect of concentrating $Na_V1.6$ in the distal AIS. Via fluorescence imaging of intracellular Na^+ concentration following single

action potentials, [28] located the greatest Na^+ influx at the middle of the AIS, whereas the distal AIS (initiation site) had only $1/4$ of this maximum. They inferred that the density of Na_V channels decreases toward the initiation site, and thus Na_V density does not determine the precise location where APs begin. Although [28] did not require $Na_V1.6$ accumulation at the distal AIS to explain the distal location of the initiation site, the authors suggest that local Na_V density can have a large effect on neuronal excitability. Temperature may also play a role in local AIS Na^+ influx measurements due to the spatial separation of Na_V subtypes. For high-speed spatiotemporal imaging of sodium influx, the pyramidal neurons in [28] and [17] were cooled to $21°C$. $Na_V1.2$ and $Na_V1.6$ differ in their responses to temperature changes [16]; thus, a deeper exploration of the effects of temperature on AP initiation is warranted. The temporal resolution of Na^+ influx measurements continues to improve: [36] achieved a resolution of $0.1ms$ imaging pyramidal cells in mouse brain slices. Another order of magnitude improvement may be sufficient to discern the local contributions of Na_V subtypes to AP initiation. The qualitative dependence of the backpropagation threshold on the somatic-versus-axonal mode of stimulation is compatible with distal AP generation as found in [28, 14] and in our work, but does not seem to rely crucially on the precise determinants of AP onset position; it relies rather on the *activation* and *availability* properties, and the kinetics of the latter.

Our model cell was kept identical in all results presented above; only the AIS was altered. Our results therefore can only be explained by the distribution of Na_V subtypes (or, the distribution of *right-shift*ed Na_V gating properties) within the AIS. Given the τ_h-dependence of the antidromic backpropagation threshold in Section 3.2.4 and the differential temperature sensitivity of $Na_V1.2$ versus $Na_V1.6$ [16], there is good reason to expect that the effects of Na_V separation predicted here will be temperature-dependent.

In summary, we have simulated a range of hypothetical Na_V distributions in the axon initial segment of a 3D-reconstructed biophysical pyramidal cell model. Our modelling shows that the spatial profile of $Na_V1.2$ and $Na_V1.6$ in the AIS and the kinetics of their *availability* and *activation* are important determinants of excitability and the backpropagation threshold. We predict that the separation of Na_V subtypes observed in early development has an asymmetrical effect on excitability which depends on whether the neuron is stimulated orthodromically or antidromically. With orthodromic stimulation, Na_V separation impedes backpropagation and reduces excitability unless the crossover is brought close to the soma. Backpropagation and excitability are both enhanced by Na_V separation when stimulation is antidromic. Maintaining a static Na_V distribution, we altered the *right-shift* of selected $Na_V1.2$ gating properties. This revealed

that steady-state *activation right-shift* controls the orthodromic backpropagation threshold, and dynamic *availability right-shift* is necessary to explain the antidromic threshold. Furthermore, given that learning is linked to backpropagation, the evolving separation of the Na_V subtypes may impact synaptic weight modification across developmental stages.

3.4 Methods

For a detailed description of the model's geometry and local membrane properties, see Supplementary Information (Section 7). We simulated a Layer 5 pyramidal neuron from cat visual cortex, modified from [25] (see SI, Section S1.1). This multicompartmental model was implemented in NEURON 8.0 [37] via Python. Every compartment has explicit intracellular and extracellular concentrations of sodium, potassium, and chloride ions. The Nernst potentials E_{Na^+}, E_{K^+}, E_{Cl^-} are calculated locally from each compartment's specific ionic concentrations, which respond to transmembrane currents. Transmembrane concentration gradients of Na^+ and K^+ are maintained via active transport (Na^+/K^+-pump), and all ions are subject to longitudinal diffusion, both intra- and extracellular, implemented using NEURON's RxD facility [38]. The cell maintains a resting potential $V_{rest} \cong -70mV$ at steady-state, and restores this state following stimulation.

In past modelling, there is sometimes a long section of bare axon following the AIS, or myelination may begin immediately at the end of the AIS. To ensure our results did not depend on this morphological feature, we ran simulations (axonal and somatic stimulation) with and without a $400\mu m$ section of bare axon separating the AIS from the first internode. The effects of Na_V distribution, summarized in Figures 2 and 4, were qualitatively identical and similar in magnitude with and without the bare axon.

3.4.1 AIS - Na_V density profiles

In our model, the density profiles of $Na_V1.2$ and $Na_V1.6$ are left- and right-handed sigmoidal functions (respectively) of normalized length s along the AIS. The proximal end of the AIS is located at $s = 0$, and the distal end is located at $s = 1$. The channel densities are expressed as maximal conductances $\bar{g}_{Na_V1.2}$ (s) and $\bar{g}_{Na_V1.6}$ (s), where the total maximal Na_V conductance $\bar{g}_{Na_V}$ is constant along the AIS:

$$\bar{g}_{Na_V} = \bar{g}_{Na_V1.2}(s) + \bar{g}_{Na_V1.6}(s) = const. \tag{2}$$

The density profiles are given by

$$\begin{cases} \bar{g}_{\mathrm{Na_V1.2}}(s) &= \dfrac{\bar{g}_{\mathrm{Na_V}}}{2}\Big(1 - x \cdot \tanh\big(\sigma(s-\kappa)\big)\Big), \\ \bar{g}_{\mathrm{Na_V1.6}}(s) &= \bar{g}_{\mathrm{Na_V}} - \bar{g}_{\mathrm{Na_V1.2}}(s) \\ &= \dfrac{\bar{g}_{\mathrm{Na_V}}}{2}\Big(1 + x \cdot \tanh\big(\sigma(s-\kappa)\big)\Big). \end{cases} \tag{3}$$

We chose the hyperbolic tangent function $\tanh(s)$, but other sigmoidal functions would do just as well. The parameter x controls the separation of the $\mathrm{Na_V}$ distribution, that is, how separated the two $\mathrm{Na_V}$ subtypes are. When $x = 0$, the distribution becomes flat —$\mathrm{Na_V1.2}$ and $\mathrm{Na_V1.6}$ are mixed uniformly along the AIS. When $x = 1$, the proximal end of the AIS contains only $\mathrm{Na_V1.2}$, and the distal end of the AIS contains only $\mathrm{Na_V1.6}$. The parameter σ is the reciprocal of the 'transition width' of the AIS $\mathrm{Na_V}$ distributions normalized by the AIS length. In all simulations shown here, $\sigma = 10.0$. Additional details are provided in Section S1.4.

3.4.2 Biophysics

Action potentials propagate via the cable equation

$$C\frac{\partial V}{\partial t} = \frac{d}{4R_a}\frac{\partial^2 V}{\partial s^2} - I_{membrane}, \tag{4}$$

where V is the membrane potential, C is the specific membrane capacitance, d is the neurite diameter, R_a is the axial resistance, s is the position along the axis of the cable, and $I_{membrane}$ is the total transmembrane current density of all ion species in the model. Each compartment has explicit intracellular and extracellular concentrations of sodium, potassium, and chloride ions. These concentrations depend on the spatial coordinate, but to simplify the notation, that is not written explicitly. We denote the intracellular/extracellular concentration of a given ionic species "Z" as $[\mathrm{Z}]_{\mathrm{in}}$, $[\mathrm{Z}]_{\mathrm{out}}$ respectively. The Nernst potentials (reversal potentials) $E_{\mathrm{Na^+}}$, $E_{\mathrm{K^+}}$, $E_{\mathrm{Cl^-}}$ of $\mathrm{Na^+}$, $\mathrm{K^+}$, and $\mathrm{Cl^-}$ are not fixed parameters but are instead determined by the intracellular and extracellular concentrations of those ions:

$$E_{\mathrm{Z}}(s) = -\frac{k_{\mathrm{B}}T}{q_{\mathrm{Z}}}\ln\left(\frac{[\mathrm{Z}]_{\mathrm{in}}}{[\mathrm{Z}]_{\mathrm{out}}}\right). \tag{5}$$

Transmembrane concentration gradients of Na^+ and K^+ are governed by active transport (Na^+/K^+-pump) and longitudinal diffusion. At each time step, ionic concentrations all over the cell are updated using transmembrane currents (Equation 8) and Fick's law. At the jth compartment this gives:

$$\begin{cases} \frac{\partial}{\partial t}[\mathrm{Z}]^j_{\mathrm{in}} = -\left(\frac{A^j}{FVol^j_{\mathrm{in}}}\right) I^j_{\mathrm{Z}} + D_{\mathrm{Z}}\nabla^2[\mathrm{Z}]^j_{\mathrm{in}} \\ \\ \frac{\partial}{\partial t}[\mathrm{Z}]^j_{\mathrm{out}} = \left(\frac{A^j}{FVol^j_{\mathrm{out}}}\right) I^j_{\mathrm{Z}} + D_{\mathrm{Z}}\nabla^2[\mathrm{Z}]^j_{\mathrm{out}}, \end{cases} \tag{6}$$

where I^j_{Z} is the transmembrane current density of ion species Z at compartment j, with Z = Cl^-, K^+, Na^+. D_{Z} denotes the diffusion coefficient of ion Z. A^j and $Vol^j_{\mathrm{in(out)}}$ are (respectively) the membrane area and intracellular/extracellular volume at the jth compartment. The total transmembrane current density at the jth compartment is

$$I^j_{membrane} = I^j_{\mathrm{Cl^-}} + I^j_{\mathrm{K^+}} + I^j_{\mathrm{Na^+}}. \tag{7}$$

Omitting the compartment index j, the specific transmembrane currents are

$$I_{membrane} : \begin{cases} I_{\mathrm{Cl^-}} = g_{\mathrm{Cl^-}}(V - E_{\mathrm{Cl^-}}) \\ I_{\mathrm{K^+}} = (g_{\mathrm{K_V}} + g_{\mathrm{K,\ leak}})(V - E_{\mathrm{K^+}}) - 2I_{pump} \\ I_{\mathrm{Na^+}} = (g_{\mathrm{Na_V}} + g_{\mathrm{Na,\ leak}})(V - E_{\mathrm{Na^+}}) + 3I_{pump}. \end{cases} \tag{8}$$

$g_{\mathrm{Cl^-}}$, $g_{\mathrm{K,\ leak}}$, and $g_{\mathrm{Na,\ leak}}$ are passive leak conductances whereas $g_{\mathrm{K_V}}$ and $g_{\mathrm{Na_V}}$ have voltage-gated Hodgkin-Huxley (HH)-style kinetics (Equation S6). Since channels are nonuniformly distributed along the cell membrane, conductances vary with location. I_{pump} is the net current produced by the Na^+/K^+-pump as a function of $[K^+]_{\mathrm{out}}$ and $[Na^+]_{\mathrm{in}}$,

$$I_{pump} = I_{maxpump}\left(1 + \frac{K_{M_{\mathrm{K^+}}}}{[\mathrm{K^+}]_{\mathrm{out}}}\right)^{-2}\left(1 + \frac{K_{M_{\mathrm{Na^+}}}}{[\mathrm{Na^+}]_{\mathrm{in}}}\right)^{-3}, \tag{9}$$

where $I_{maxpump}$ controls the maximal pump current, $K_{M_{\mathrm{K^+}}}$ and $K_{M_{\mathrm{Na^+}}}$ are Michaelis-Menten kinetic constants, and the Na^+ and K^+ currents flowing through the pump are $I_{\mathrm{Na^+},pump} = 3I_{pump}$ and $I_{\mathrm{K^+},pump} =$

$-2I_{pump}$.

3.4.3 Shift-Clamping and the Hodgkin-Huxley model

In the Hodgkin-Huxley model [34] a gating variable u evolves according to its voltage-dependent forward and backward transition rates $\alpha_u(V)$ and $\beta_u(V)$ as

$$\frac{du}{dt} = \alpha_u(V)[1-u] - \beta_u(V)u, \tag{10}$$

where u could be $\mathrm{Na_V}$ *activation* m or *availability* h, or $\mathrm{K_V}$ *activation* n, etc. This can be rewritten using the steady-state $u_\infty(V)$ and voltage-dependent time constant $\tau_u(V)$ of the gating variable

$$\frac{du}{dt} = \frac{u_\infty(V) - u}{\tau_u(V)}, \tag{11}$$

where u_∞ and τ_u are computed from α_u and β_u via

$$u_\infty(V) = \frac{\alpha_u(V)}{\alpha_u(V) + \beta_u(V)} \quad \text{and} \quad \tau_u(V) = \frac{1}{\alpha_u(V) + \beta_u(V)} \quad . \tag{12}$$

When shifting the voltage-dependence of u_∞ by ΔV_{RS}, it is natural to assume that one should apply the same shift to τ_u given Equation 12, since u_∞ and τ_u are both functions of $\alpha_u(V)$ and $\beta_u(V)$ in such models. However, our simulations can shift $u_\infty(V)$ or $\tau_u(V)$ independently of one another: e.g. $\tau'_u(V) = \tau_u(V - \Delta V_{\mathrm{RS}})$, $u'_\infty(V) = u_\infty(V)$. The forward and backward rates become

$$\alpha'_u = \frac{u'_\infty(V)}{\tau'_u(V)} \quad \text{and} \quad \beta'_u = \frac{1 - u'_\infty(V)}{\tau'_u(V)}. \tag{13}$$

Putting this to use, one can modify the *right-shift* of combinations of

$$\left\{\tau_h^{\mathrm{Na_V1.2}}(V),\ h_\infty^{\mathrm{Na_V1.2}}(V),\ \tau_m^{\mathrm{Na_V1.2}}(V),\ m_\infty^{\mathrm{Na_V1.2}}(V)\right\}, \tag{14}$$

by adding "$-\Delta V_{\mathrm{RS}}$" to the argument of the selected variables' $u_\infty(V)$s or $\tau_u(V)$s.

3.4.4 Data availability

The simulation software that produces the results in this paper and the plotted data will be made available on ModelDB at http://modeldb.yale.edu/267088. Also, the Supplementary Information includes tables of parameters that detail the model setup.

3.4.5 Code availability

Model code will be posted on ModelDB upon publication at http://modeldb.yale.edu/267088.

4 Acknowledgments

We acknowledge the support of the Natural Sciences and Engineering Research Council of Canada (NSERC), to BJ and AL. We wish to thank: Catherine E. Morris, for directing our attention to the AIS. Nicholas T. Carnevale and Robert A. McDougal, for generously helping us to solve a number of model implementation problems using NEURON. We also thank Louis Jacques for helpful discussion.

5 Author contributions

B. Barlow: conceptualization, model development, implementing the models and curating the outputs, coding, optimizing, model validation, figure preparation, and manuscript writing and revising; A. Longtin: conceptualization, model development, model validation, manuscript editing; and B. Joós: conceptualization, model development, model validation, manuscript editing. B. Joós and A. Longtin jointly supervised this work.

6 Competing interests

The authors declare no competing interests.

References

[1] Debanne D, Campanac E, Bialowas A, Carlier E, Alcaraz G. Axon Physiology. Physiological Reviews. 2011 Apr;91(2):555-602. Available from: https://journals.physiology.org/doi/full/10.1152/physrev.00048.2009.

[2] Adachi R, Yamada R, Kuba H. Plasticity of the Axonal Trigger Zone. Neuroscientist. 2015 Jun;21(3):255-65. Available from: https://doi.org/10.1177/1073858414535986.

[3] Gulledge AT, Bravo JJ. Neuron Morphology Influences Axon Initial Segment Plasticity. eNeuro. 2016 Jan;3(1). Available from: https://www.eneuro.org/content/3/1/ENEURO.0085-15.2016.

[4] Verbist C, Müller MG, Mansvelder HD, Legenstein R, Giugliano M. The location of the axon initial segment affects the bandwidth of spike initiation dynamics. PLOS Computational Biology. 2020 Jul;16(7):e1008087. Available from: https://journals.plos.org/ploscompbiol/article?id=10.1371/journal.pcbi.1008087.

[5] Franken TP, Bondy BJ, Haimes DB, Goldwyn JH, Golding NL, Smith PH, et al. Glycinergic axonal inhibition subserves acute spatial sensitivity to sudden increases in sound intensity. eLife. 2021 Jun;10:e62183. Available from: https://elifesciences.org/articles/62183.

[6] Petersen AV, Cotel F, Perrier JF. Plasticity of the Axon Initial Segment: Fast and Slow Processes with Multiple Functional Roles. Neuroscientist. 2017 Aug;23(4):364-73. Available from: https://doi.org/10.1177/1073858416648311.

[7] Vrselja Z, Daniele SG, Silbereis J, Talpo F, Morozov YM, Sousa AMM, et al. Restoration of brain circulation and cellular functions hours post-mortem. Nature. 2019 Apr;568(7752):336-43. Available from: https://www.nature.com/articles/s41586-019-1099-1.

[8] Shepherd GM, Marenco L, Hines ML, Migliore M, McDougal RA, Carnevale NT, et al. Neuron Names: A Gene- and Property-Based Name Format, With Special Reference to Cortical Neurons. Frontiers in Neuroanatomy. 2019;13. Available from: https://www.frontiersin.org/article/10.3389/fnana.2019.00025.

[9] Kole MHP, Stuart GJ. Signal Processing in the Axon Initial Segment. Neuron. 2012 Jan;73(2):235-47. Available from: https://www.sciencedirect.com/science/article/pii/S0896627312000505.

[10] Höfflin F, Jack A, Riedel C, Mack-Bucher J, Roos J, Corcelli C, et al. Heterogeneity of the Axon Initial Segment in Interneurons and Pyramidal Cells of Rodent Visual Cortex. Frontiers in Cellular Neuroscience. 2017;11:332. Available from: https://www.frontiersin.org/article/10.3389/fncel.2017.00332.

[11] Mainen ZF, Joerges J, Huguenard JR, Sejnowski TJ. A model of spike initiation in neocortical pyramidal neurons. Neuron. 1995 Dec;15(6):1427-39. Available from: https://www.sciencedirect.com/science/article/pii/0896627395900209.

[12] Kole MHP, Ilschner SU, Kampa BM, Williams SR, Ruben PC, Stuart GJ. Action potential generation requires a high sodium channel density in the axon initial segment. Nat Neurosci. 2008 Feb;11(2):178-86. Available from: https://www.nature.com/articles/nn2040.

[13] Brette R. Sharpness of Spike Initiation in Neurons Explained by Compartmentalization. PLOS Computational Biology. 2013 Dec;9(12):e1003338. Available from: https://journals.plos.org/ploscompbiol/article?id=10.1371/journal.pcbi.1003338.

[14] Hu W, Tian C, Li T, Yang M, Hou H, Shu Y. Distinct contributions of Nav1.6 and Nav1.2 in action potential initiation and backpropagation. Nat Neurosci. 2009 Aug;12(8):996-1002. Available from: https://www.nature.com/articles/nn.2359.

[15] Tian C, Wang K, Ke W, Guo H, Shu Y. Molecular identity of axonal sodium channels in human cortical pyramidal cells. Front Cell Neurosci. 2014 Sep;8. Available from: http://journal.frontiersin.org/article/10.3389/fncel.2014.00297/abstract.

[16] Ye M, Yang J, Tian C, Zhu Q, Yin L, Jiang S, et al. Differential roles of NaV1.2 and NaV1.6 in regulating neuronal excitability at febrile temperature and distinct contributions to febrile seizures. Sci Rep. 2018 Dec;8(1):753. Available from: http://www.nature.com/articles/s41598-017-17344-8.

[17] Katz E, Stoler O, Scheller A, Khrapunsky Y, Goebbels S, Kirchhoff F, et al. Role of sodium channel subtype in action potential generation by neocortical pyramidal neurons. PNAS. 2018 Jul;115(30):E7184-92. Available from: https://www.pnas.org/content/115/30/E7184.

[18] Spratt PWE, Alexander RPD, Ben-Shalom R, Sahagun A, Kyoung H, Keeshen CM, et al. Paradoxical hyperexcitability from NaV1.2 sodium channel loss in neocortical pyramidal cells. Cell Reports. 2021 Aug;36(5). Available from: https://www.cell.com/cell-reports/abstract/S2211-1247(21)00910-4.

[19] Liu H, Wang HG, Pitt G, Liu Z. Direct Observation of Compartment-Specific Localization and Dynamics of Voltage-Gated Sodium Channels. J Neurosci. 2022 Jul;42(28):5482-98. Available from: https://www.jneurosci.org/lookup/doi/10.1523/JNEUROSCI.0086-22.2022.

[20] Rush AM, Dib-Hajj SD, Waxman SG. Electrophysiological properties of two axonal sodium channels, Na $_{v}$ 1.2 and Na $_{v}$ 1.6, expressed in mouse spinal sensory neurones: Sodium channels in sensory neurones. The Journal of Physiology. 2005 May;564(3):803-15. Available from: https://onlinelibrary.wiley.com/doi/10.1113/jphysiol.2005.083089.

[21] Ben-Shalom R, Keeshen CM, Berrios KN, An JY, Sanders SJ, Bender KJ. Opposing Effects on Na V 1.2 Function Underlie Differences Between SCN2A Variants Observed in Individuals With Autism Spectrum Disorder or Infantile Seizures. Biological Psychiatry. 2017 Aug;82(3):224-32. Available from: https://linkinghub.elsevier.com/retrieve/pii/S0006322317300410.

[22] Feldman D. The Spike-Timing Dependence of Plasticity. Neuron. 2012 Aug;75(4):556-71. Available from: https://linkinghub.elsevier.com/retrieve/pii/S0896627312007039.

[23] Regehr WG, Carey MR, Best AR. Activity-Dependent Regulation of Synapses by Retrograde Messengers. Neuron. 2009 Jul;63(2):154-70. Available from: https://www.sciencedirect.com/science/article/pii/S0896627309005078.

[24] Spratt PWE, Ben-Shalom R, Keeshen CM, Burke KJ, Clarkson RL, Sanders SJ, et al. The Autism-Associated Gene Scn2a Contributes to Dendritic Excitability and Synaptic Function in the Prefrontal Cortex. Neuron. 2019 Aug;103(4):673-85.e5. Available from: https://linkinghub.elsevier.com/retrieve/pii/S0896627319304908.

[25] Mainen ZF, Sejnowski TJ. Influence of dendritic structure on firing pattern in model neocortical neurons. Nature. 1996 Jul;382(6589):363-6. Available from: https://www.nature.com/articles/382363a0.

[26] Doiron B, Longtin A, Turner RW, Maler L. Model of Gamma Frequency Burst Discharge Generated by Conditional Backpropagation. Journal of Neurophysiology. 2001 Oct;86(4):1523-45. Available from: https://journals.physiology.org/doi/full/10.1152/jn.2001.86.4.1523.

[27] Payeur A, Guerguiev J, Zenke F, Richards BA, Naud R. Burst-dependent synaptic plasticity can coordinate learning in hierarchical circuits. Nat Neurosci. 2021 Jul;24(7):1010-9. Available from: https://www.nature.com/articles/s41593-021-00857-x.

[28] Baranauskas G, David Y, Fleidervish IA. Spatial mismatch between the Na+ flux and spike initiation in axon initial segment. PNAS. 2013 Jan. Available from: https://www.pnas.org/content/early/2013/01/17/1215125110.

[29] Hu W, Shu Y. Axonal bleb recording. Neurosci Bull. 2012 Aug;28(4):342-50. Available from: https://link.springer.com/article/10.1007/s12264-012-1247-1.

[30] Wang JA, Lin W, Morris T, Banderali U, Juranka PF, Morris CE. Membrane trauma and Na+ leak from Nav1.6 channels. American Journal of Physiology-Cell Physiology. 2009 Oct;297(4):C823-34. Available from: https://journals.physiology.org/doi/full/10.1152/ajpcell.00505.2008.

[31] Yin L, Rasch MJ, He Q, Wu S, Dou F, Shu Y. Selective Modulation of Axonal Sodium Channel Subtypes by 5-HT $_{1A}$ Receptor in Cortical Pyramidal Neuron. Cereb Cortex. 2015 Oct:bhv245. Available from: https://academic.oup.com/cercor/article-lookup/doi/10.1093/cercor/bhv245.

[32] Boucher PA, Joós B, Morris CE. Coupled left-shift of Nav channels: modeling the Na+-loading and dysfunctional excitability of damaged axons. J Comput Neurosci. 2012 Oct;33(2):301-19. Available from: https://doi.org/10.1007/s10827-012-0387-7.

[33] Joos B, Barlow BM, Morris CE. Calculating the Consequences of Left-Shifted Nav Channel Activity in Sick Excitable Cells. In: Chahine M, editor. Voltage-gated Sodium Channels: Structure, Function and Channelopathies. vol. 246. Cham: Springer International Publishing; 2017. p. 401-22. Series Title:

Handbook of Experimental Pharmacology. Available from: http://link.springer.com/10.1007/164_2017_63.

[34] Hodgkin AL, Huxley AF. A quantitative description of membrane current and its application to conduction and excitation in nerve. The Journal of Physiology. 1952;117(4):500-44. Available from: https://onlinelibrary.wiley.com/doi/abs/10.1113/jphysiol.1952.sp004764.

[35] Ma Y, Huguenard JR. Reemerging role of cable properties in action potential initiation. PNAS. 2013 Mar;110(10):3715-6. Available from: https://www.pnas.org/content/110/10/3715.

[36] Filipis L, Canepari M. Optical measurement of physiological sodium currents in the axon initial segment. J Physiol. 2021 Jan;599(1):49-66. Available from: https://onlinelibrary.wiley.com/doi/10.1113/JP280554.

[37] Carnevale NT, Hines ML. The NEURON book. Cambridge, UK ; New York: Cambridge University Press; 2006.

[38] McDougal RA, Hines ML, Lytton WW. Reaction-diffusion in the NEURON simulator. Front Neuroinform. 2013;7. Available from: http://journal.frontiersin.org/article/10.3389/fninf.2013.00028/abstract.

[39] Samson E, Marchand J, Snyder KA. Calculation of ionic diffusion coefficients on the basis of migration test results. Mat Struct. 2003 Apr;36(3):156-65. Available from: https://link.springer.com/article/10.1007/BF02479554.

7 Supplementary information

Contents

S1.1 Model: pyramidal cell geometry . . . 33
S1.2 Spikes and Backpropagation in the Model . . . 33
S1.3 Additional Simulations . . . 34
S1.4 AIS - technical details . . . 38
S1.5 Voltage-Gated Channels . . . 40
S1.5.1 Defining V_{RS}: the *right-shift* of $\mathrm{Na_V1.2}$ . . . 41
S1.5.2 Notation: V_{RS}, ΔV_{RS} . . . 42
S1.5.3 Space plots of $\mathrm{Na_V}$ kinetics along the AIS — steady-state . . . 43
S1.6 Diffusion Coefficients . . . 45
S1.7 Tables of parameters . . . 46

S1.1 Model: pyramidal cell geometry

Figure S1 displays the neuron used in this paper. The dendritic morphology is a digital reconstruction of a Layer 5 pyramidal neuron from cat visual cortex, modified from [25]. These neurons have dendrites roughly as tall as the thickness of the cortex (several mm) and axon initial segment length similar to the width of a human hair (tens of μm [9]).

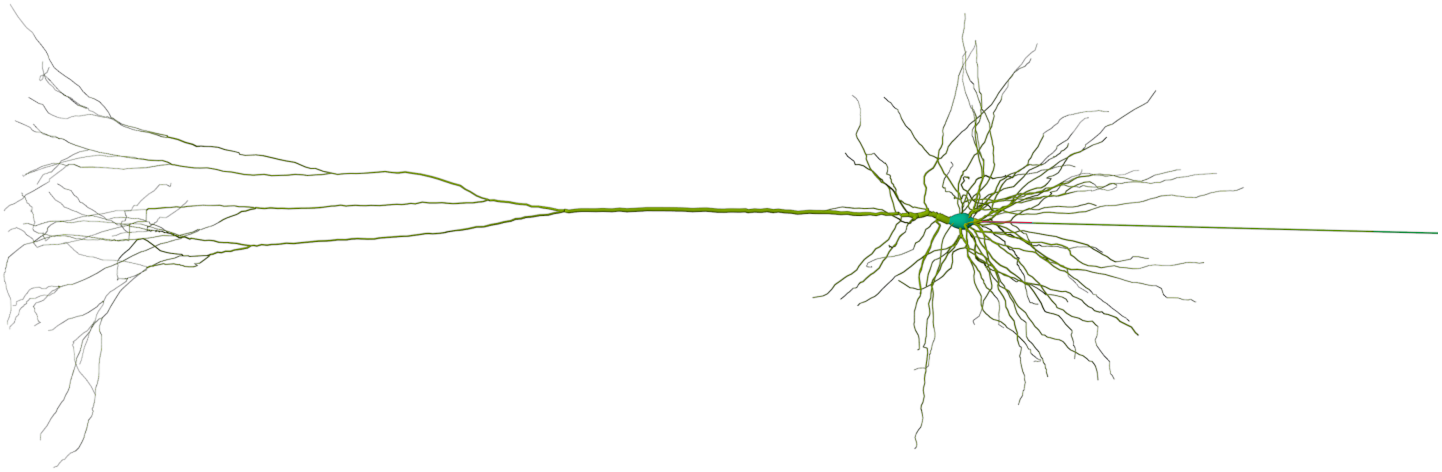

Figure S1: Geometry of the model cell: Layer 5 pyramidal neuron from cat visual cortex, modified from [25]. Somatodendritic morphology is digitally reconstructed from a real cell; hillock, AIS, and axon are added. Image created using blenderNEURON: blenderNEURON.org, blender.org.

The same reconstructed cell geometry was used in [14]. A cylindrical axon similar to that used in [14] was attached to the reconstructed soma by a $10\mu m$ long tapered hillock. The axon proper includes fifteen nodes of Ranvier (pink dots on the axon in Figure S2) separated by myelinated $100\mu m$ internodes. The axon initial segment length was set to $\ell = 25.0\mu m$, consistent with [10]. Voltage-gated channels are present all over the cell. Channel densities and passive leaks are given as conductances. The local conductances vary with position —representative values have been tabulated in Section S1.7.

S1.2 Spikes and Backpropagation in the Model

When pyramidal cells spike, the action potential can travel backward into the dendrites. This phenomenon is called backpropagation. For example, Figure S2 illustrates spikes with and without backpropagation. Peak voltage is recorded across the entire cell model. The peak voltage at the tips of the dendrites is indicated in orange and has a higher amplitude consistent with the sealed-end effect. Backpropagation

was deemed to have occurred when the mean peak voltage of dendritic tips exceeded $-10.0mV$ following stimulation.

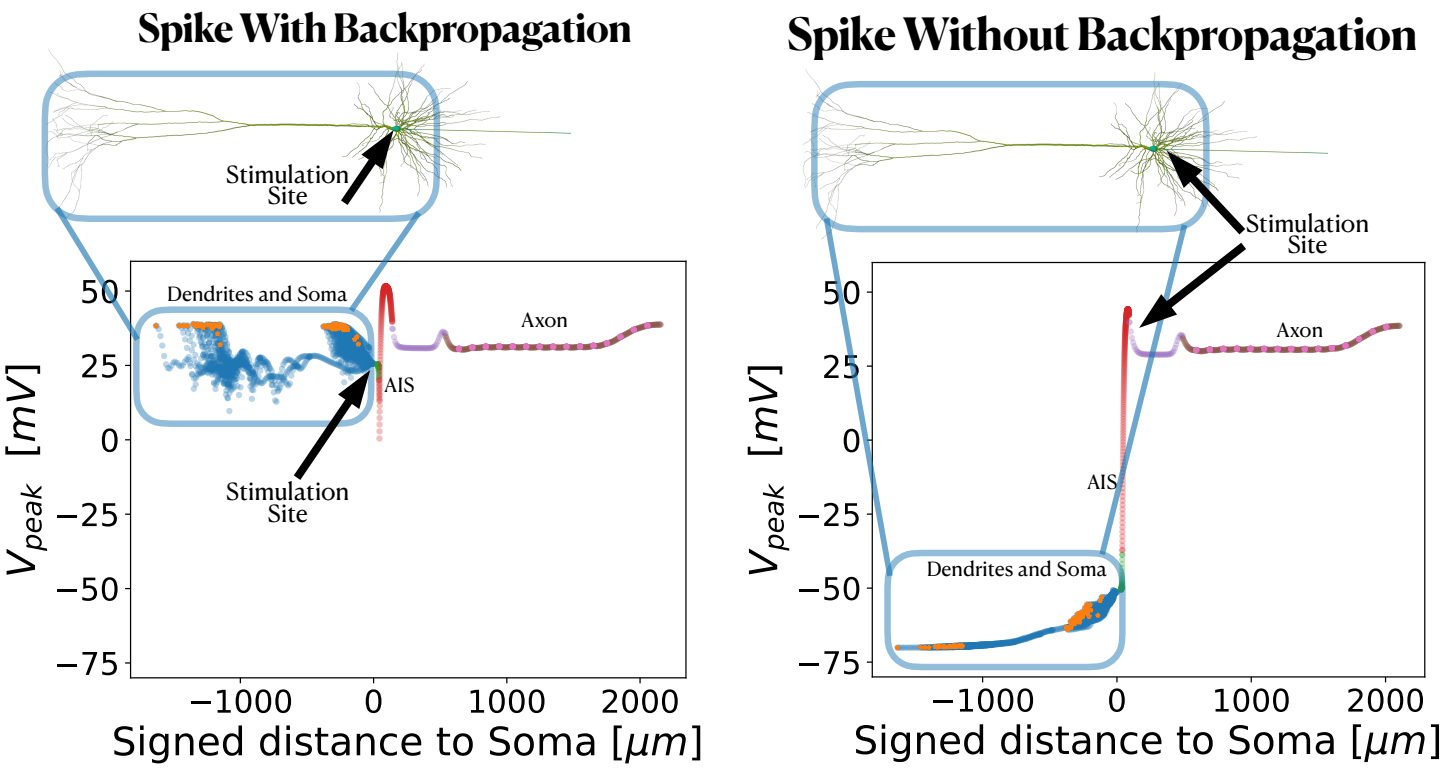

Figure S2: Spikes with and without backpropagation: Beginning on the right-hand side: an action potential (AP) has occurred following axonal stimulation (current injected just distal to the AIS). Note that the peak voltage in the soma and dendrites remains near the resting potential $\approx -70mV$, indicating that backpropagation did not occur. We call this scenario where an AP has been sent down the axon orthodromically from the stimulation site (i.e. to the right in this panel) without a somatodendritic spike "forward propagation" or "forwardprop". To the left is an AP that backpropagated: the entire cell spiked, in this case following somatic stimulation; backpropagation can also occur following axonal stimulation. The somatodendritic peak voltages are indicated by a blue box in each case. This and similar figures are inspired by "Figure 4" of [11].

S1.3 Additional Simulations

In the main text, we found that with a $25\mu m$ AIS, the slope of I_{BP} versus x for somatic stimulation became flat around $\kappa \approx 0.4$, which is $20\mu m$ away from the soma since $L_{\text{hillock}} = 10\mu m$ (Figure 2). In Figure S3, with a $100\mu m$ AIS, the I_{BP} slope flattens around $\kappa \approx 0.1$, which again corresponds to a distance of roughly $20\mu m$ from the soma since the distance in μm to the crossover position is $\kappa \times \ell_{\text{AIS}}$. This suggests that the threshold-lowering effect of Na_V separation for small κ (Figure 2) results from the increased proximal

density of $Na_V1.6$ when the crossover is brought near to the soma —and is not due to the proximal density of $Na_V1.2$, consistent with Figure S4.

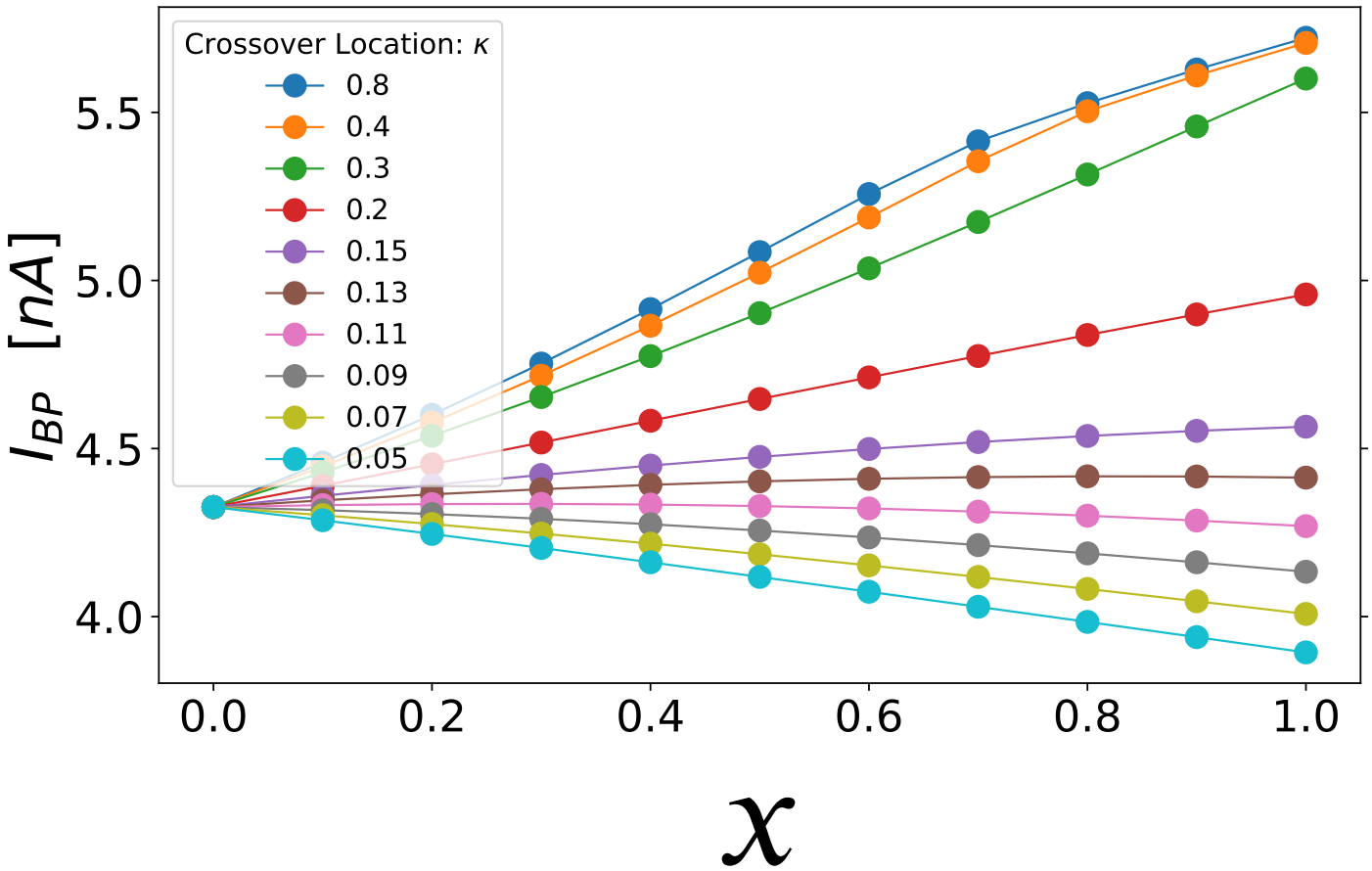

Figure S3: Somatic Stimulation with AIS lengthened to $100\mu m$ (compare with Figure 2 in the main text where the AIS length was $25\mu m$): Combined effect of varying crossover location (κ) and Na_V separation (x) in the axon initial segment. The distance in μm to the crossover position is $\kappa \times \ell_{AIS}$. The lines have been drawn to guide the eye.

Figure S4 demonstrates that increasing κ raises the backpropagation threshold when current is injected somatodendritically (orthodromic stimulation), even when the slopes in Figure 2 are negative. Increasing κ means moving the Na_V crossover location away from the soma, which increases the proportion of $Na_V1.2$ (versus $Na_V1.6$) in the AIS; see Figure 1b.

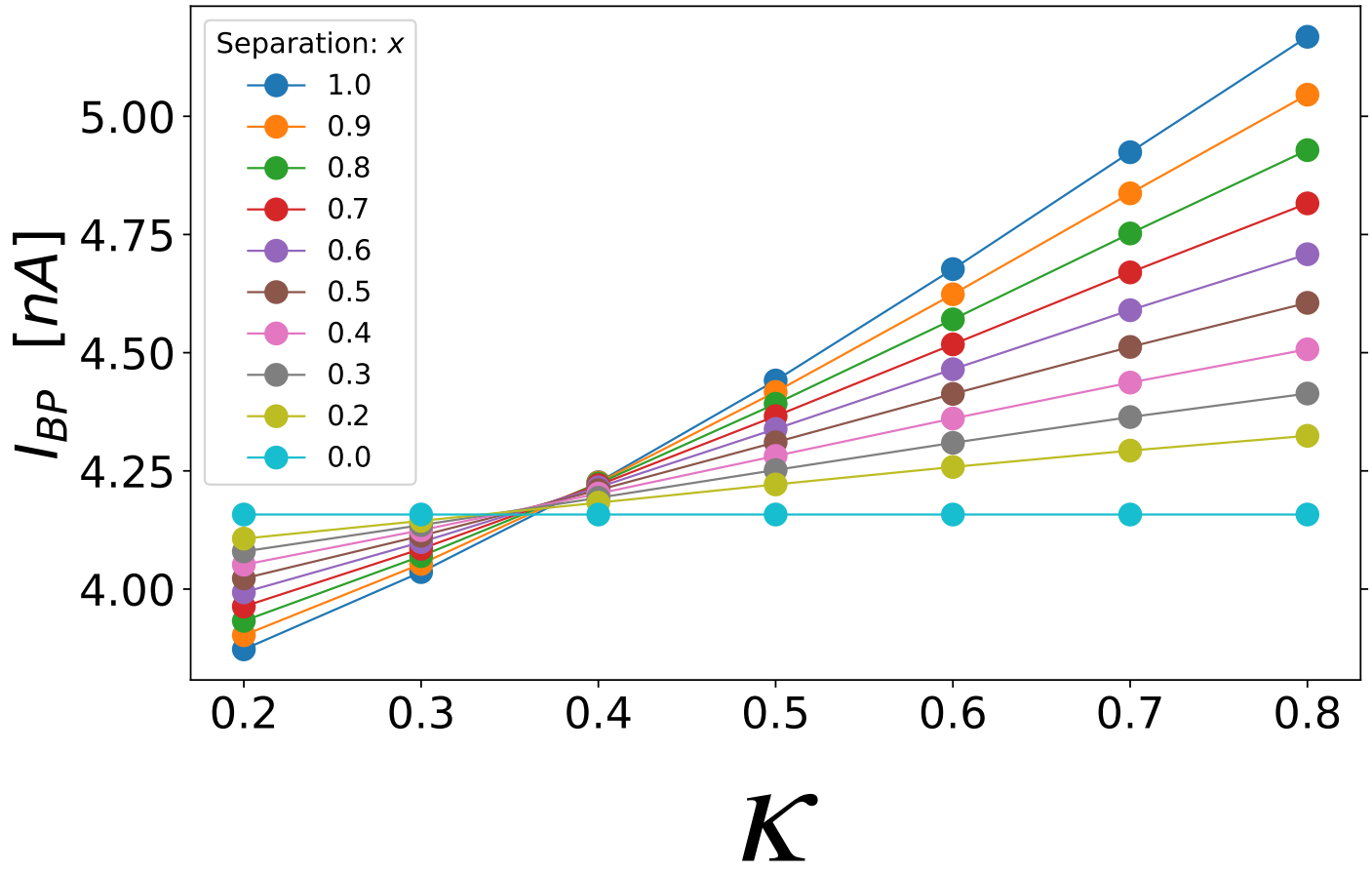

Figure S4: Somatic Stimulation with nominal AIS length ($\ell_{\text{AIS}} = 25.0\mu m$). The combined effect of varying crossover location (κ) and Na_V separation (x) in the axon initial segment. Increasing κ raises the backpropagation threshold. Here the abscissa is the normalized crossover position κ, instead of Na_V separation (compare with Figure 2). In Figure 2, all curves converge at $x = 0$. Here, that intersection point is replaced by the $x = 0$ *line*. Notice that every $x > 0$ curve has a positive slope: the backpropagation threshold I_{BP} *increases* with κ. Increasing κ when $x > 0$ necessarily increases the ratio of $\text{Na}_\text{V}1.2$ conductance to $\text{Na}_\text{V}1.6$ conductance in the AIS (see Equation S1). It follows that concentrating $\text{Na}_\text{V}1.2$ in the proximal AIS raises the backpropagation threshold, for somatic stimulation. The lines have been drawn to guide the eye.

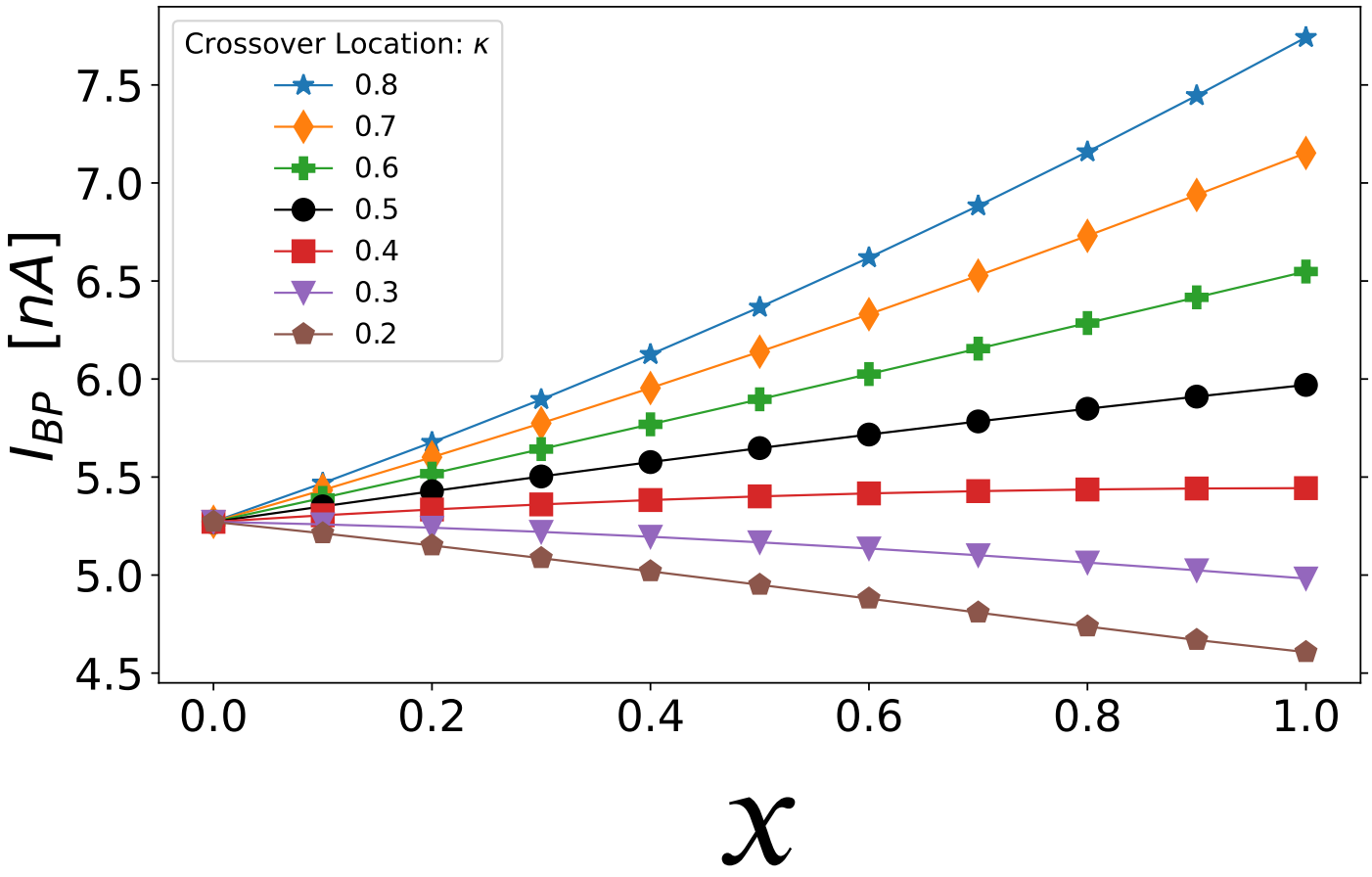

Figure S5: Dendritic Stimulation with nominal AIS length ($\ell_{\text{AIS}} = 25.0\mu m$). Current injection at the main apical dendrite yields the same qualitative behaviour as for somatic stimulation. Compare with (Figure 2). Varying the separation parameter "x" from $x = 0$ to $x = 1$, the distribution of Na_V channels goes from flat (homogeneous) to separated, the latter approximating the distribution observed in developing pyramidal neurons (see Figure 1a). Note that curves for all values of κ converge to a single point at $x = 0$ since κ can have no effect when the two Na_V's are uniformly distributed along the AIS. The lines have been drawn to guide the eye.

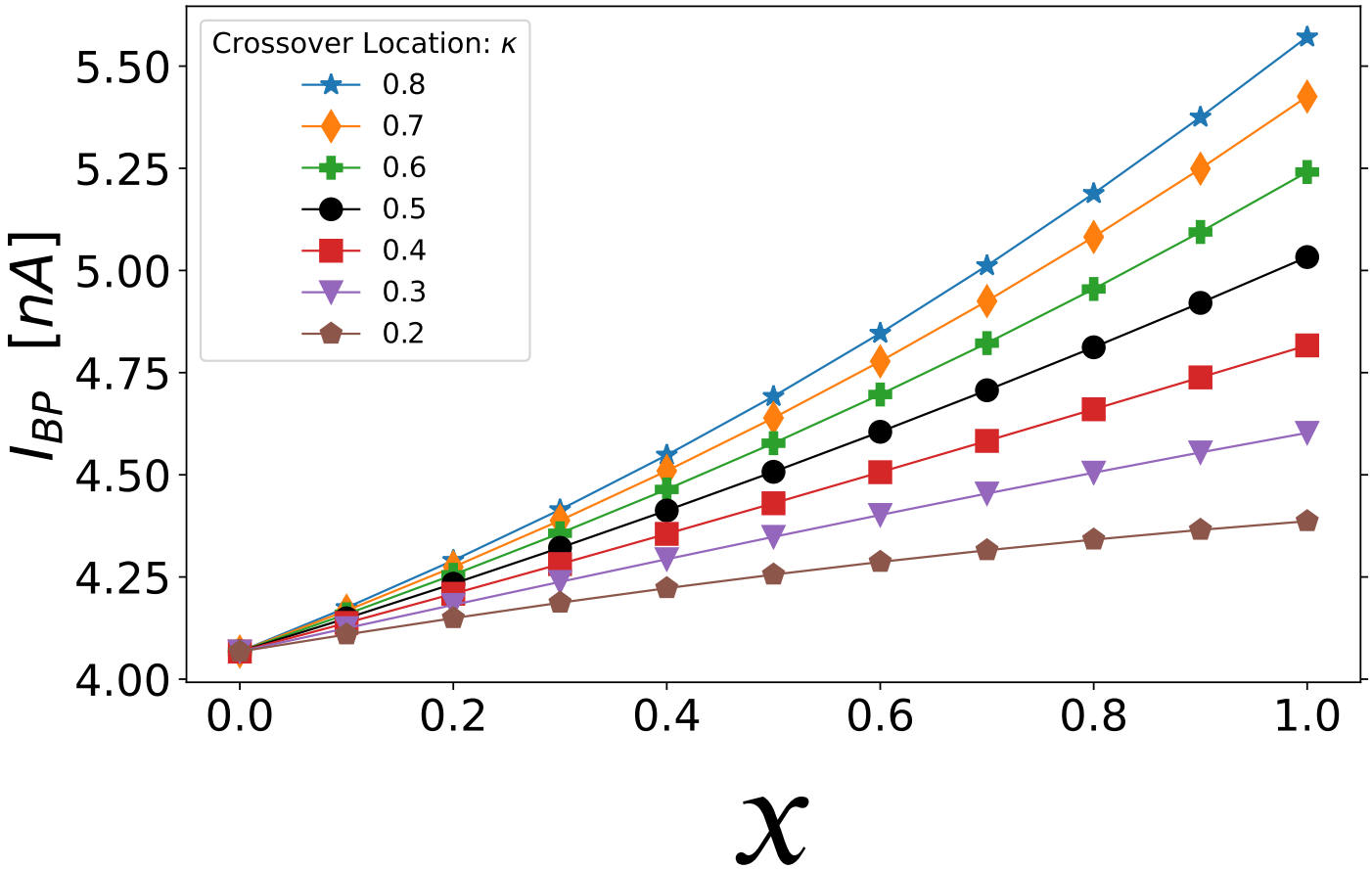

Figure S6: Somatic Stimulation: lengthening the hillock to $30\mu m$ removes the negative slopes observed in Figure 2 and Figure S3. In all other plots, we have used $L_{\text{hillock}} = 10\mu m$. AIS length is $\ell_{\text{AIS}} = 25.0\mu m$ as in all other plots unless indicated otherwise. The lines have been drawn to guide the eye.

S1.4 AIS - technical details

In our model, the density profiles of $\text{Na}_\text{V}1.2$ and $\text{Na}_\text{V}1.6$ are left- and right-handed sigmoidal functions (respectively) of normalized length s along the AIS. The proximal end of the AIS is located at $s = 0$, and the distal end is located at $s = 1$. The channel densities are expressed as maximal conductances $\bar{g}_{\text{Na}_\text{V}1.2}$ (s) and $\bar{g}_{\text{Na}_\text{V}1.6}$ (s), where the total maximal Na_V conductance $\bar{g}_{\text{Na}_\text{V}}$ is constant along the AIS:

$$\bar{g}_{\text{Na}_\text{V}} = \bar{g}_{\text{Na}_\text{V}1.2}(s) + \bar{g}_{\text{Na}_\text{V}1.6}(s) = const. \tag{S1}$$

The density profiles are given by

$$\begin{cases} \bar{g}_{\mathrm{Na_V1.2}}(s) &= \dfrac{\bar{g}_{\mathrm{Na_V}}}{2}\Big(1 - x \cdot \tanh\big(\sigma(s-\kappa)\big)\Big), \\ \bar{g}_{\mathrm{Na_V1.6}}(s) &= \bar{g}_{\mathrm{Na_V}} - \bar{g}_{\mathrm{Na_V1.2}}(s) \\ &= \dfrac{\bar{g}_{\mathrm{Na_V}}}{2}\Big(1 + x \cdot \tanh\big(\sigma(s-\kappa)\big)\Big). \end{cases} \tag{S2}$$

We chose the hyperbolic tangent function $\tanh(s)$, but other sigmoidal functions would do just as well. The parameter x controls the separation of the $\mathrm{Na_V}$ distribution, that is, how separated the two $\mathrm{Na_V}$ subtypes are. When $x = 0$, the distribution becomes flat —$\mathrm{Na_V1.2}$ and $\mathrm{Na_V1.6}$ are mixed uniformly along the AIS. When $x = 1$, the proximal end of the AIS contains only $\mathrm{Na_V1.2}$, and the distal end of the AIS contains only $\mathrm{Na_V1.6}$. The parameter σ is the reciprocal of the 'transition width' of the AIS $\mathrm{Na_V}$ distributions normalized by the AIS length. In all simulations shown here, $\sigma = 10.0$.

The total $\mathrm{Na_V}$ conductance of the AIS is proportional to AIS length ℓ since its diameter is constant

$$\bar{G}_{\mathrm{Na_V}} = \bar{g}_{\mathrm{Na_V}} \cdot (\text{Area of AIS}) \propto \bar{g}_{\mathrm{Na_V}}\,\ell_{\mathrm{AIS}}. \tag{S3}$$

The contribution to this total conductance from $\mathrm{Na_V1.2}$ is

$$\bar{G}_{\mathrm{Na_V1.2}} \propto \int_0^{\ell_{\mathrm{AIS}}} d\ell'\, \bar{g}_{\mathrm{Na_V1.2}}(\ell') = \ell_{\mathrm{AIS}} \int_0^1 ds\, \frac{\bar{g}_{\mathrm{Na_V}}}{2}\Big(1 - x \cdot \tanh\big(\sigma(s-\kappa)\big)\Big), \tag{S4}$$

$$\Longrightarrow \bar{G}_{\mathrm{Na_V1.2}} \propto 1 - x \cdot \underbrace{\left(\frac{\ln\big(\cosh(\sigma) - \sinh(\sigma)\tanh(\sigma\kappa)\big)}{\sigma}\right)}_{\text{“}M\text{”}}. \tag{S5}$$

The root of the term labeled "M" in Equation S5 is $\kappa = \frac{1}{2}$, and the slope of M is negative: $M(\kappa < 0.5) > 0$, $M(\kappa > 0.5) < 0$. Since $M(\kappa = 0.5) = 0$, the derivative of $\bar{G}_{\mathrm{Na_V1.2}}$ (and $\bar{G}_{\mathrm{Na_V1.6}}$) with respect to x is zero when the crossover is located in the middle of the AIS, which is the standard configuration for varying $\mathrm{Na_V}$ separation. We call $\kappa = 0.5$ standard because, in this configuration, the effects on the backpropagation threshold due to varying x can not be due to changes in the total conductance of $\mathrm{Na_V1.6}$ or $\mathrm{Na_V1.2}$ in the AIS. In other words, the results of sweeping x from 0 to 1 with κ fixed at 0.5 in Figure 4, Figure 5, and

Figure 2 are purely due to mixing and separating $\mathrm{Na_V}1.6$ from $\mathrm{Na_V}1.2$ in the AIS.

Since by definition $0 \leqslant \kappa \leqslant 1$ and $\sigma > 0$, the partial derivative of M with respect to κ is negative. It follows from Equation S5 that $\bar{G}_{\mathrm{Na_V}1.2}$ increases as the crossover position is moved distally. Likewise $\bar{G}_{\mathrm{Na_V}1.6}$ decreases with increasing κ.

S1.5 Voltage-Gated Channels

The voltage-gated sodium and potassium conductances $g_{\mathrm{Na_V}}(V,t)$ and $g_{\mathrm{K_V}}(V,t)$ in Equation 8 are modeled using HH-style kinetics [34] fitted to mammalian pyramidal cell data by [11], and then further adapted by [14] to include two $\mathrm{Na_V}$ variants (Equation S7). In the Hodgkin-Huxley model, the current density I_{Z} of ion species "Z" through voltage-gated channels of a given type is

$$I_{\mathrm{Z_V}} = \bar{g}_{\mathrm{Z_V}} m^p h^q (V - E_{\mathrm{Z}}), \tag{S6}$$

where $\bar{g}$ is the maximal conductance, $m(V,t)$ is the probability for an *activation* gate to be open, p is the number of *activation* gates per channel, $h(V,t)$ is the *availability* (probability that the channel is *not inactivated*), and q is the number of inactivation gates per channel. $\mathrm{Na_V}$ channels are modeled as having three *activation* gates ($p = 3$) and a single inactivation gate ($q = 1$) so that $g_{\mathrm{Na_V}} \propto m^3 h$. Likewise, $\mathrm{K_V}$ channels have a single *activation* gate and no inactivation ($g_{\mathrm{K_V}} \propto n$). The gating variables m, h, and n evolve according to Equations 10, 11, and 12. Since the cell features two $\mathrm{Na_V}$ subtypes ($\mathrm{Na_V}1.2$ and $\mathrm{Na_V}1.6$), the model computes two sets of sodium *activation* and *availability* variables. The current density I_{Na} through the $\mathrm{Na_V}$ channels is then

$$I_{\mathrm{Na_V}} = \left(\underbrace{\bar{g}_{\mathrm{Na_V}1.2} (m^{\mathrm{Na_V}1.2})^3 h^{\mathrm{Na_V}1.2}}_{g_{\mathrm{Na_V}1.2}} + \underbrace{\bar{g}_{\mathrm{Na_V}1.6} (m^{\mathrm{Na_V}1.6})^3 h^{\mathrm{Na_V}1.6}}_{g_{\mathrm{Na_V}1.6}} \right) (V - E_{\mathrm{Na^+}}), \tag{S7}$$

where $g_{\mathrm{Na_V}1.2} + g_{\mathrm{Na_V}1.6} = g_{\mathrm{Na_V}}$ in Equation 8.

Figure S7 plots the voltage-dependent kinetics of $m^{\mathrm{Na_V}1.2}$, $h^{\mathrm{Na_V}1.2}$, $m^{\mathrm{Na_V}1.6}$ and $h^{\mathrm{Na_V}1.6}$. The steady-state *activation* and *availability* functions and their voltage-sensitive time constants were implemented using the parameters provided in [14] and in model code published by [25]. We further modified the channel models to allow shift-clamping; see Section 3.2.4 and Section 3.4.3.

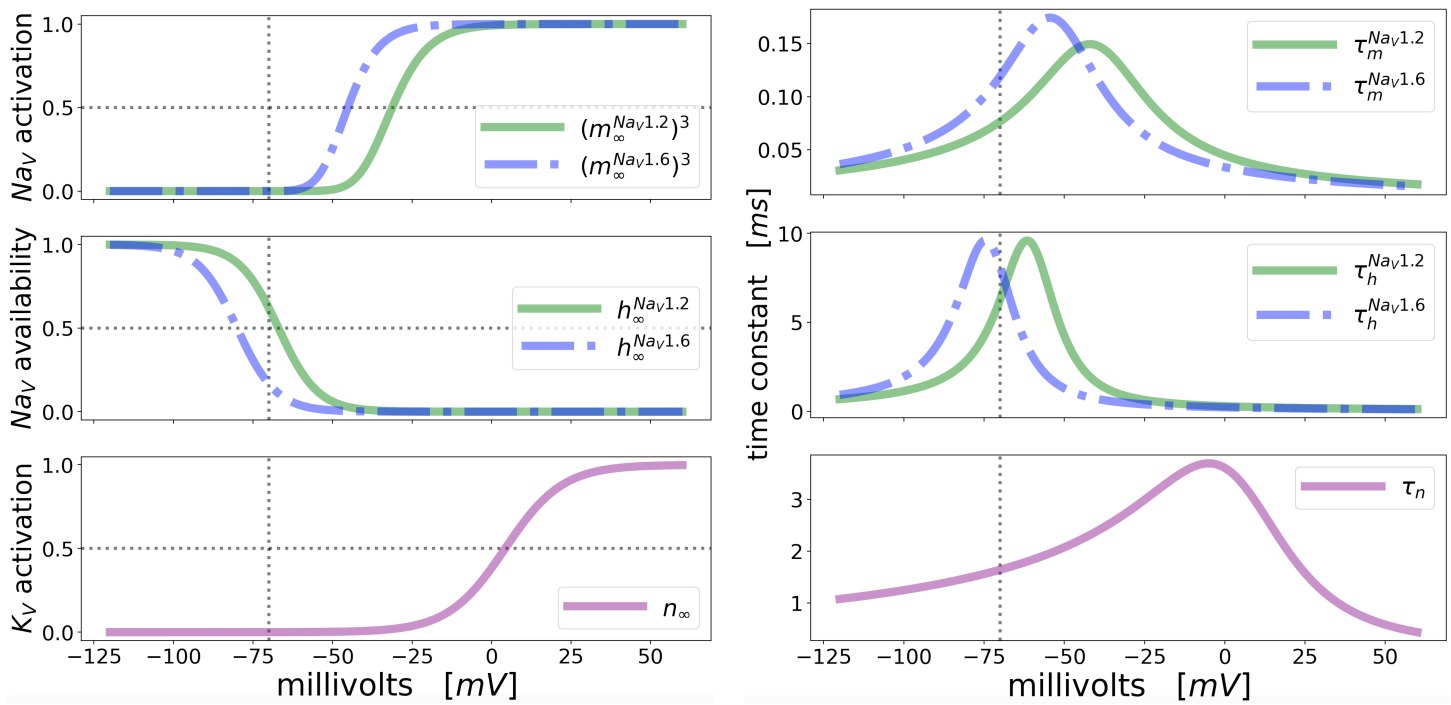

(a) (b)

Figure S7: Gating properties of the voltage-gated sodium and potassium channels that are implemented in this model. Dotted vertical lines indicate the resting potential V_{rest}. (a) Steady-state *activation* and *availability* curves for $\text{Na}_\text{V}1.2$ and $\text{Na}_\text{V}1.6$, and steady-state K_V *activation*. (b) Voltage-sensitive time constants of $\text{Na}_\text{V}1.2$, $\text{Na}_\text{V}1.6$, and K_V. $\text{Na}_\text{V}1.2$ is *right-shift*ed by an amount V_{RS} relative to $\text{Na}_\text{V}1.6$ (defined in Section S1.5.1). In this model, $V_{\text{RS}} = 13.0mV$.

The *right-shift* of $\text{Na}_\text{V}1.2$ (defined mathematically in Section S1.5.1) is easiest to observe in the top two plots of Figure S7a. Steady-state *activation* $\left(m_\infty^{\text{Na}_\text{V}1.2}(V)\right)^3$ and *availability* $h_\infty^{\text{Na}_\text{V}1.2}(V)$ curves of $\text{Na}_\text{V}1.2$ are plotted as solid green lines, and dashed blue lines are the corresponding curves for $\text{Na}_\text{V}1.6$. The voltage shift separating Na_V *activation* curves is approximately V_{RS}, though it varies with position since the gating variables of Na_V *activation* ($m^{\text{Na}_\text{V}1.2}$, $m^{\text{Na}_\text{V}1.6}$) are raised to the third power and do not have identical slopes [14]. However, the *availability* curves are much easier to compare: in this model, $h_\infty^{\text{Na}_\text{V}1.2}(V)$ is shifted exactly $V_{\text{RS}} = 13.0mV$ to the right of $h_\infty^{\text{Na}_\text{V}1.6}(V)$. The *right-shift* of $\text{Na}_\text{V}1.2$ is also visible in the voltage-sensitive time constants (Figure S7b).

S1.5.1 Defining V_{RS}: the *right-shift* of $\text{Na}_\text{V}1.2$

V_{RS} is a parameter in this model representing the experimentally measured depolarizing shift in the voltage dependence of $\text{Na}_\text{V}1.2$ *activation* and inactivation kinetics, relative to $\text{Na}_\text{V}1.6$ kinetics. Because V_{RS} is

empirical, it is fixed in this paper.

We define the $\mathrm{Na_V1.6}$ half-*activation* voltage $V_{1/2}^{\mathrm{Na_V1.6}}$ as the voltage at which a single $\mathrm{Na_V1.6}$ *activation* gate (randomly selected from an ensemble of gates held at $V = V_{1/2}^{\mathrm{Na_V1.6}}$) has a 50% chance of being in the open state:

$$m_\infty^{\mathrm{Na_V1.6}}(V_{1/2}^{\mathrm{Na_V1.6}}) \stackrel{\text{def}}{=} \frac{1}{2}.$$

Although the kinetics of $\mathrm{Na_V1.2}$ differ from $\mathrm{Na_V1.6}$ kinetics in ways *other than right-shift*, we can now use $V_{1/2}^{\mathrm{Na_V1.6}}$ to define V_{RS} as the voltage that satisfies

$$\boxed{m_\infty^{\mathrm{Na_V1.2}}(V_{1/2}^{\mathrm{Na_V1.6}} + V_{\mathrm{RS}}) = m_\infty^{\mathrm{Na_V1.6}}(V_{1/2}^{\mathrm{Na_V1.6}}) = \frac{1}{2}}. \tag{S8}$$

Note that $V_{1/2}^{\mathrm{Na_V1.6}}$ and V_{RS} are unique since m_∞ is monotonically increasing. Equation S8 also contains the half-*activation* voltage for $\mathrm{Na_V1.2}$,

$$\left(V_{1/2}^{\mathrm{Na_V1.6}} + V_{\mathrm{RS}}\right) = V_{1/2}^{\mathrm{Na_V1.2}}, \tag{S9}$$

which is depolarized or "right-shifted" by an amount V_{RS} relative to $\mathrm{Na_V1.6}$ (see Figure S7).

To simulate alterations to $\mathrm{Na_V1.2}$ *right-shift* in our shift-clamping method, we use another parameter called ΔV_{RS}, which is not based on experiment. Although the $\mathrm{Na_V1.2}$ *right-shift* is not a high precision measurement ($V_{\mathrm{RS}} \sim 10{-}15mV$), the *parameter* V_{RS} is kept fixed in our model for conceptual purposes: we find it helpful to distinguish empirical parameters (like V_{RS}) from exploratory parameters that intentionally deviate from experiment (like ΔV_{RS}). In fact, we use ΔV_{RS} to selectively change the model's $\mathrm{Na_V}$ kinetics to explain the effects of $\mathrm{Na_V}$ distribution on excitability in terms of the lengthwise distribution of gating properties (see Section 3.2.4 and Section 3.4.3).

S1.5.2 Notation: V_{RS}, ΔV_{RS}

In our notation, V_{RS} is *not written explicitly* in the argument of $\mathrm{Na_V1.2}$ gating variables or their time constants. Instead, we write

$$\tau_h^{\mathrm{Na_V1.2}}(V),\ \tau_h^{\mathrm{Na_V1.6}}(V),\ \text{et cetera},$$

and let the superscript "$\mathrm{Na_V1.2}$" indicate that $\tau_h^{\mathrm{Na_V1.2}}$ is *right-shift*ed relative to $\tau_h^{\mathrm{Na_V1.6}}$, from the fact that $\mathrm{Na_V1.2}$ channels are *right-shift*ed in this model.

However, the parameter ΔV_{RS} *is* written explicitly in the argument when we model the effects of modifying the *right-shift* (Figure 6: shift-clamping). For example, when applying $\Delta V_{\mathrm{RS}} \neq 0$ to the *selected* kinetic variables $\tau_h^{\mathrm{Na_V1.2}}$ and $m_\infty^{\mathrm{Na_V1.2}}$, we would write

$$\begin{cases} \tau_h^{\mathrm{Na_V1.2}} = \tau_h^{\mathrm{Na_V1.2}}(V - \Delta V_{\mathrm{RS}}) \\ h_\infty^{\mathrm{Na_V1.2}} = h_\infty^{\mathrm{Na_V1.2}}(V) \\ \tau_m^{\mathrm{Na_V1.2}} = \tau_m^{\mathrm{Na_V1.2}}(V) \\ m_\infty^{\mathrm{Na_V1.2}} = m_\infty^{\mathrm{Na_V1.2}}(V - \Delta V_{\mathrm{RS}}). \end{cases} \tag{S10}$$

Using this notation, positive values of ΔV_{RS} will shift kinetic curves to the right (depolarizing shift), and negative ΔV_{RS} produces a hyperpolarizing shift.

S1.5.3 Space plots of $\mathrm{Na_V}$ kinetics along the AIS — steady-state

The distribution of $\mathrm{Na_V1.2}$ and $\mathrm{Na_V1.6}$ in the AIS creates a lengthwise distribution of gating properties. Proximal $\mathrm{Na_V1.2}$ increases local steady-state *availability*, owing to these channels' *right-shift* (V_{RS}). In Figure S8a we visualize this effect using $\mathcal{H}(s)$: the net *availability* of $\mathrm{Na_V}$s ($\mathcal{H}$) as a function of position (s), computed by weighting $h^{\mathrm{Na_V1.2}}$ and $h^{\mathrm{Na_V1.6}}$ according to their respective local $\mathrm{Na_V}$ channel densities:

$$\mathcal{H}(s,t) = \frac{\bar{g}_{\mathrm{Na_V1.2}}(s) h^{\mathrm{Na_V1.2}}(s,t) + \bar{g}_{\mathrm{Na_V1.6}}(s) h^{\mathrm{Na_V1.6}}(s,t)}{\bar{g}_{\mathrm{Na_V1.2}}(s) + \bar{g}_{\mathrm{Na_V1.6}}(s)}. \tag{S11}$$

An effective local $\mathrm{Na_V}$ time constant of *availability* ($\boldsymbol{\mathcal{T}}$) can be computed from $\tau_h^{\mathrm{Na_V1.2}}$ and $\tau_h^{\mathrm{Na_V1.6}}$ as

$$\boldsymbol{\mathcal{T}}(s,t) = \frac{\bar{g}_{\mathrm{Na_V1.2}}(s) \tau_h^{\mathrm{Na_V1.2}}(s,t) + \bar{g}_{\mathrm{Na_V1.6}}(s) \tau_h^{\mathrm{Na_V1.6}}(s,t)}{\bar{g}_{\mathrm{Na_V1.2}}(s) + \bar{g}_{\mathrm{Na_V1.6}}(s)}. \tag{S12}$$

Above, we have abbreviated

$$f(V(s,t),t) = f(s,t) \text{ for } f = h^{\mathrm{Na_V1.2}}, h^{\mathrm{Na_V1.6}}, \tau_h^{\mathrm{Na_V1.2}}, \tau_h^{\mathrm{Na_V1.6}}. \tag{S13}$$

In Figure S8b we have selectively disabled the *right-shift* of $\tau_h^{\mathrm{Na_V1.2}}$ by setting $\Delta V_{\mathrm{RS}} = -V_{\mathrm{RS}} = -13.0mV$

in Equation 1, which leaves the *right-shift* of steady-state *availability* unchanged.

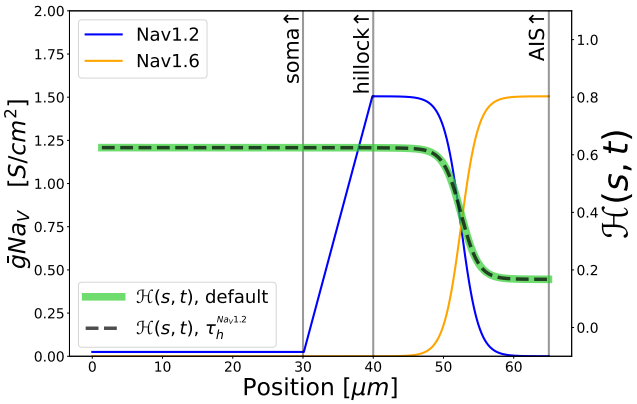

(a) Solid green curve: nominal $Na_V1.2$ *right-shift*. Travelling from left to right across the AIS, $Na_V1.6$ overtakes $Na_V1.2$ as a share of the total local Na_V density. The accompanying change in Na_V *right-shift* causes $\mathcal{H}(s)$ to drop from ≈ 0.6 at the soma and proximal AIS, down to ≈ 0.2 at the distal AIS and axon. Dashed black curve: the *right-shift* of $\tau_h^{Na_V1.2}$ has been selectively disabled without altering $h_\infty^{Na_V1.2}$, and thereby $\mathcal{H}$ is also unaffected. See (b) to the right as well as Equation 1.

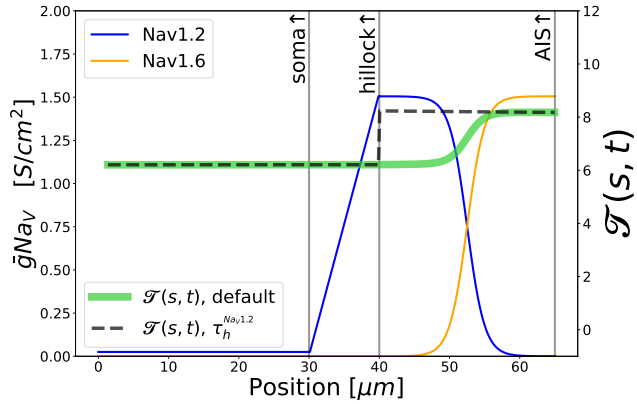

(b) Solid green curve: nominal $Na_V1.2$ *right-shift*. Where $Na_V1.6$ overtakes $Na_V1.2$ as a share of the total local Na_V density, $\boldsymbol{\mathcal{T}}(s)$ increases from $\approx 6ms$ to $\approx 8ms$. Dashed black curve: *right-shift* of $\tau_h^{Na_V1.2}$ selectively disabled by setting $\Delta V_{RS} = -V_{RS}$ in Equation 1. The effective time constant of Na_V *availability* $\boldsymbol{\mathcal{T}}(s)$ is now uniform along the AIS. The abrupt transition in $\boldsymbol{\mathcal{T}}$ at the AIS-hillock interface —instead of the smooth transition along the AIS in the green curve— is due to the *right-shift* of $\tau_h^{Na_V1.2}(V)$ being selectively disabled —see Equation S12. The *right-shift* of $h_\infty^{Na_V1.2}(V)$ has not been altered (see Equation S11), and the corresponding $\mathcal{H}$ (dashed black) curve in (a) is unchanged —hence the term "selective".

Figure S8: The effect of $Na_V1.2$ *right-shift* on local Na_V *availability* along the cell is visible in space plots of steady-state total *availability* $\mathcal{H}(s)$ (a) and total time constant $\boldsymbol{\mathcal{T}}(s)$ (b) at $V = V_{rest}$. See Equation S11 and Equation S12, respectively.

S1.6 Diffusion Coefficients

Diffusion coefficients for Na^+, K^+, and Cl^- in water at 25.0 ℃ are provided by [39] :

$$\begin{cases} D_{\mathrm{Na}^+} = 1.334 \times 10^{-9} \dfrac{m^2}{s} \\ D_{\mathrm{K}^+} = 1.957 \times 10^{-9} \dfrac{m^2}{s} \\ D_{\mathrm{Cl}^-} = 2.032 \times 10^{-9} \dfrac{m^2}{s}. \end{cases} \tag{S14}$$

Our simulations are done at a warmer temperature, so these coefficients need to be adjusted. We make the adjustment using the Stokes-Einstein equation

$$D = \frac{k_B T}{\zeta(T)} = \frac{k_B T}{6\pi r \eta(T)} \; ; \tag{S15}$$

where k_B is Boltzmann's constant, T is the temperature (Kelvins K), and ζ is called the drag coefficient. ζ is given by the ion's radius r and the viscosity $\eta(T)$ of the medium (liquid water), which depends on temperature. Hence the ratio of diffusion coefficients for ion species Z at T_2 and T_1 is

$$\frac{D_{\mathrm{Z}}(T_2)}{D_{\mathrm{Z}}(T_1)} = \left(\frac{T_2}{T_1}\right)\left(\frac{\eta(T_1)}{\eta(T_2)}\right), \tag{S16}$$

with T_2 and T_1 converted to K. The reference values provided by [39] are measured at $298.15K$ (25.0℃), and the simulation temperature is $310.15K$ (37.0℃). Assuming the viscosity of water, we have $\eta(T_1) \cong 0.89\ mPa\ s$ and $\eta(T_2) \cong 0.691\ mPa\ s$. Substituting these η's into Equation S16 gives for each ionic species Z

$$\underbrace{D_{\mathrm{Z}}(310.15K)}_{37.0℃} \cong 1.34 \times \underbrace{D_{\mathrm{Z}}(298.15K)}_{25.0℃}, \tag{S17}$$

which yields the temperature-adjusted diffusion coefficients

$$\begin{cases} D_{\mathrm{Na}^+} = 1.79 \times 10^{-9} \dfrac{m^2}{s} \\ D_{\mathrm{K}^+} = 2.62 \times 10^{-9} \dfrac{m^2}{s} \\ D_{\mathrm{Cl}^-} = 2.72 \times 10^{-9} \dfrac{m^2}{s}. \end{cases} \tag{S18}$$

S1.7 Tables of parameters

In the following tables, we compare our model to previous models on which it is based ([11], [25], [14]). At different locations in the cell, we list key parameter values from these papers alongside our own. We also include certain measurements (membrane potential, ion concentrations, Nernst potentials) taken from our model at each location once the cell has equilibrated.

The following symbols are used in the tables: (Units are given in the tables.)

"×" This symbol appears when a parameter is not featured in the model corresponding to a given column.

$V_{\mathbf{rest}}$ Resting potential. The transmembrane voltage of the model neuron at steady-state with no injected current.

$V_{\mathbf{m}}^{\mathbf{location}}$ Transmembrane voltage at 'location'. In our model, the steady-state transmembrane voltage is actively maintained everywhere by Na^+/K^+-pumps and longitudinal diffusion, which control the explicit intracellular and extracellular ion concentrations. As such, the tabulated values are *recorded* from the model, not parameters per se. In the other models listed, V_{m} is identical to V_{rest}.

$R_{\mathbf{axial}}$ Axial resistance. The resistance to axial current flow across a compartment is R_{axial} multiplied by the compartment length, divided by the compartment's cross-sectional area.

$D_{\mathbf{ion}}$ Diffusion coefficient of the specified ion in water at $37°\mathrm{C}$.

$T_{\mathbf{ref}}$ Reference temperature of experimentally developed channel properties used in the models. Past modelling, on which this paper is based, used temperature factors (described below) to adjust channel densities and speed up channel kinetics to warmer temperatures.

T Simulation temperature.

$Q_{\bar{g}_{\mathbf{V}}}^{\mathbf{Mainen}} = Q_{10,\bar{g}_{\mathbf{V}}}^{(T-T_{\mathbf{ref}})/10°\mathrm{C}}$ To adjust for a warmer simulation temperature of $T = 37°\mathrm{C}$ [25] scales up the maximal voltage-gated conductances, which were originally developed at $T = 23°\mathrm{C}$ ([11]), by a factor which we denote $Q_{\mathrm{Mainen}}^{\bar{g}_{\mathrm{V}}}$. The authors warn in their model code that this scaling is valid only at $37°\mathrm{C}$ and state that their program is not designed to model other temperatures. This internal temperature scaling can accidentally obscure parameter settings when one attempts to borrow parameters separately from the past code or from later papers that reuse these channel models. For this reason, we

have removed the temperature scaling from our own model code by setting our reference temperature equal to the simulation temperature, which sets $Q^{\bar{g}_{\mathrm{V}}}_{\mathrm{Mainen}} = 1$.

$\bar{g}^{\mathbf{location}}_{\mathbf{Na_V \cdot Total}}$ Total combined maximal voltage-gated conductance density of $\mathrm{Na_V1.2}$ and $\mathrm{Na_V1.6}$ at the specified 'location' in the cell (see Equation S1). The location can be an entire Section if the membrane properties are uniform (in NEURON, Sections consist of multiple compartments). For example, this model has uniform somatodendritic channel densities, so 'soma' is sufficient to specify those parameters.

$\bar{g}^{\mathbf{location}}_{\mathbf{K_V \cdot Total}}$ Maximal voltage-gated K^+ conductance density at the specified 'location'.

$C_{\mathbf{m}}$ Membrane capacitance per unit area. Applies everywhere except at internodes.

$C^{\mathbf{myelin}}_{\mathbf{m}}$ Membrane capacitance of myelinated internodes.

$L_{\mathbf{Section}}$ Length of the specified 'Section' (soma, hillock, AIS, etc.)

$d^{\mathbf{position\ within\ Section}}_{\mathbf{Section}}$ Diameter at a given normalized position $(0 \leqslant s \leqslant 1)$ within the specified Section (soma, hillock, AIS, etc.). The position is not specified when the diameter is uniform.

$R^{\mathbf{Section}}_{\mathbf{Passive}}$ Membrane resistivity in 'Section'.

$g^{\mathbf{Section}}_{\mathbf{Passive}}$ Passive generic transmembrane leak conductance density in 'Section'.

$g^{\mathbf{Section}}_{\mathbf{Ion,\ leak}}$ Specific leak conductance density of 'Ion' in 'Section'.

$I^{\mathbf{Section}}_{\mathbf{MaxPump}}$ Maximum Na^+/K^+-pump current density in 'Section'.

$E^{\mathbf{Section}}_{\mathbf{current\ type}}$ Nernst Potential (reversal potential) of transmembrane current 'current type' (e.g. 'leak') in 'Section' (e.g. 'soma').

$[\mathbf{Ion}]^{\mathbf{Section}}_{\mathbf{in/out}}$ Intracellular ('in') or Extracellular ('out') concentration of 'Ion' at 'Section', with the neuron at steady-state. Because these concentrations are maintained by Na^+/K^+-pumps and longitudinal diffusion in our model, the concentrations tabulated here are measurements *recorded* from the simulation at steady-state, rather than being fixed parameters.

ranvier0, myelin0: In our model, there are 15 nodes of Ranvier and 16 myelinated internodes. The Section named 'ranvier0' is the first node of Ranvier. And 'myelin0' is the first myelinated internode of the axon, located between the distal end of the AIS (or the distal end of the bare axon when that is included) and the proximal end of ranvier0.

Type	Parameter Name	OurModel	Mainen95	Mainen96	Hu2009	units
Global						
	V_{rest}	-70.0	-70.0	-70.0	-70.0	mV
	R_{axial}	150	200	150	150	$\Omega \cdot cm$
	D_{Cl^-}	2.72	×	×	×	$10^{-9}\frac{m^2}{s}$
	D_{Na^+}	1.79	×	×	×	$10^{-9}\frac{m^2}{s}$
	D_{K^+}	2.62	×	×	×	$10^{-9}\frac{m^2}{s}$
	T_{ref}	37.0	23.0	23.0	23.0	℃
	T	37.0	23.0	37.0	37.0	℃
	$Q_{\bar{g}_{\text{V}}}^{\text{Mainen}} = Q_{10,\bar{g}_{\text{V}}}^{(T-T_{\text{ref}})/10℃}$	1.0	1.0	3.21	3.21	dimensionless
	C_{m}	0.75	0.75	0.75	1.0	$\frac{\mu F}{cm^2}$
	$C_{\text{m}}^{\text{myelin}}$	0.02	0.04	0.02	0.02	$\frac{\mu F}{cm^2}$

Geometry

	L_{soma}	30.0	25.8	30.0	30.0	μm
	L_{hillock}	10.0	10.0	10.0	10.0	μm
	L_{AIS}	100.0	15.0	15.0	50.0	μm
	$L_{\text{bare·axon}}$	400	×	×	400	μm
	$d^{0.5}_{\text{soma}}$	19.38	15.2	19.0	19.0	μm
	$d^{1.0}_{\text{soma}}$	8.62	15.2	8.6	8.6	μm
	$d^{0.0}_{\text{hillock}}$	8.62	4.0	4.0	3.8	μm
	$d^{1.0}_{\text{hillock}}$	1.22	1.0	1.0	2.4	μm
	d_{AIS}	1.22	1.0	1.0	1.22	μm
	$d_{\text{bare·axon}}$	1.22	×	×	1.02	μm
section	Parameter Name	OurModel	Mainen95	Mainen96	Hu2009	units
soma						
	$\bar{g}^{\text{soma}}_{\text{Na}_\text{V}\cdot\text{Total}}$	2.51×10^{-2}	0.003	0.002	0.008	$\frac{S}{cm^2}$
	$\bar{g}^{\text{soma}}_{\text{Na}_\text{V}\cdot\text{Total}} \times Q^{\text{Mainen}}_{\bar{g}_\text{V}}$	2.51×10^{-2}	3.00×10^{-3}	6.42×10^{-3}	2.57×10^{-2}	$\frac{S}{cm^2}$

$\bar{g}_{\mathrm{K_V}}^{\mathrm{soma}}$	7.53×10^{-3}	0.01	0.02	0.002	$\frac{S}{cm^2}$
$\bar{g}_{\mathrm{K_V}}^{\mathrm{soma}} \times Q_{\bar{g}_{\mathrm{V}}}^{\mathrm{Mainen}}$	7.53×10^{-3}	1.00×10^{-2}	6.42×10^{-2}	6.42×10^{-3}	$\frac{S}{cm^2}$
$R_{\mathrm{Passive}}^{\mathrm{soma}}$	7.16×10^{3}	4.00×10^{4}	3.00×10^{4}	3.00×10^{4}	$\Omega \cdot cm^2$
$g_{\mathrm{Passive}}^{\mathrm{soma}}$	1.40×10^{-4}	2.50×10^{-5}	3.33×10^{-5}	3.33×10^{-5}	$\frac{S}{cm^2}$
$g_{\mathrm{Cl^-,\ leak}}^{\mathrm{soma}}$	2.09×10^{-5}	$\times$	$\times$	$\times$	$\frac{S}{cm^2}$
$g_{\mathrm{Na^+,\ leak}}^{\mathrm{soma}}$	2.23×10^{-5}	$\times$	$\times$	$\times$	$\frac{S}{cm^2}$
$g_{\mathrm{K^+,\ leak}}^{\mathrm{soma}}$	9.66×10^{-5}	$\times$	$\times$	$\times$	$\frac{S}{cm^2}$
$I_{\mathrm{MaxPump}}^{\mathrm{soma}}$	1.33×10^{-2}	$\times$	$\times$	$\times$	$\frac{mA}{cm^2}$
$V_{\mathrm{m}}^{\mathrm{soma}}$	-70.2	-70.0	-70.0	-70.0	mV
$E_{\mathrm{leak}}^{\mathrm{soma}}$	$\times$	-70.0	-70.0	-70.0	mV
$E_{\mathrm{Cl}}^{\mathrm{soma}}$	-70.0	$\times$	$\times$	$\times$	mV
$E_{\mathrm{Na}}^{\mathrm{soma}}$	60.0	60.0	50.0	60.0	mV
$E_{\mathrm{K}}^{\mathrm{soma}}$	-90.0	-90.0	-90.0	-90.0	mV
$[\mathrm{Cl^-}]_{\mathrm{in}}^{\mathrm{soma}}$	11.0	$\times$	$\times$	$\times$	mM
$[\mathrm{Cl^-}]_{\mathrm{out}}^{\mathrm{soma}}$	151.0	$\times$	$\times$	$\times$	mM

	$[\mathrm{Na}^+]_{\mathrm{in}}^{\mathrm{soma}}$	15.0	×	×	×	mM
	$[\mathrm{Na}^+]_{\mathrm{out}}^{\mathrm{soma}}$	141.6	×	×	×	mM
	$[\mathrm{K}^+]_{\mathrm{in}}^{\mathrm{soma}}$	140.0	×	×	×	mM
	$[\mathrm{K}^+]_{\mathrm{out}}^{\mathrm{soma}}$	4.8	×	×	×	mM
section	Parameter Name	OurModel	Mainen95	Mainen96	Hu2009	units
AIS						
	$\bar{g}_{\mathrm{Na_V}\cdot\mathrm{Total}}^{\mathrm{AIS}}$	1.505	3.0	3.0	0.32	$\frac{S}{cm^2}$
	$\bar{g}_{\mathrm{Na_V}\cdot\mathrm{Total}}^{\mathrm{AIS}} \times Q_{\bar{g}_{\mathrm{V}}}^{\mathrm{Mainen}}$	1.505	3.0	9.628	1.027	$\frac{S}{cm^2}$
	$\bar{g}_{\mathrm{K_V}}^{\mathrm{AIS}}$	4.52×10^{-1}	×	0.2	0.1	$\frac{S}{cm^2}$
	$\bar{g}_{\mathrm{K_V}}^{\mathrm{AIS}} \times Q_{\bar{g}_{\mathrm{V}}}^{\mathrm{Mainen}}$	4.52×10^{-1}	×	6.42×10^{-1}	3.21×10^{-1}	$\frac{S}{cm^2}$
	$R_{\mathrm{Passive}}^{\mathrm{AIS}}$	4.77×10^{1}	5.00×10^{1}	5.00×10^{1}	5.00×10^{1}	$\Omega \cdot cm^2$
	$g_{\mathrm{Passive}}^{\mathrm{AIS}}$	2.10×10^{-2}	2.00×10^{-2}	2.00×10^{-2}	2.00×10^{-2}	$\frac{S}{cm^2}$
	$g_{\mathrm{Cl^-,\ leak}}^{\mathrm{AIS}}$	3.14×10^{-3}	×	×	×	$\frac{S}{cm^2}$
	$g_{\mathrm{Na^+,\ leak}}^{\mathrm{AIS}}$	3.34×10^{-3}	×	×	×	$\frac{S}{cm^2}$

	$g^{\mathrm{AIS}}_{\mathrm{K^+,\ leak}}$	1.45×10^{-2}	×	×	×	$\frac{S}{cm^2}$
	$I^{\mathrm{AIS}}_{\mathrm{MaxPump}}$	1.995	×	×	×	$\frac{mA}{cm^2}$
	$V^{\mathrm{AIS}}_{\mathrm{m}}$	−69.9	−70.0	−70.0	−70.0	mV
	$E^{\mathrm{AIS}}_{\mathrm{leak}}$	×	−70.0	−70.0	−70.0	mV
	$E^{\mathrm{AIS}}_{\mathrm{Cl}}$	−70.0	×	×	×	mV
	$E^{\mathrm{AIS}}_{\mathrm{Na}}$	59.9	60.0	50.0	60.0	mV
	$E^{\mathrm{AIS}}_{\mathrm{K}}$	−90.0	−90.0	−90.0	−90.0	mV
	$[\mathrm{Cl^-}]^{\mathrm{AIS}}_{\mathrm{in}}$	11.0	×	×	×	mM
	$[\mathrm{Cl^-}]^{\mathrm{AIS}}_{\mathrm{out}}$	151.0	×	×	×	mM
	$[\mathrm{Na^+}]^{\mathrm{AIS}}_{\mathrm{in}}$	15.1	×	×	×	mM
	$[\mathrm{Na^+}]^{\mathrm{AIS}}_{\mathrm{out}}$	141.6	×	×	×	mM
	$[\mathrm{K^+}]^{\mathrm{AIS}}_{\mathrm{in}}$	139.9	×	×	×	mM
	$[\mathrm{K^+}]^{\mathrm{AIS}}_{\mathrm{out}}$	4.8	×	×	×	mM

section	Parameter Name	OurModel	Mainen95	Mainen96	Hu2009	units
myelin0						

$\bar{g}^{\text{myelin0}}_{\text{Na}_\text{V}\cdot\text{Total}}$	1.61×10^{-2}	0.003	$\times$	0.002	$\frac{S}{cm^2}$
$\bar{g}^{\text{myelin0}}_{\text{Na}_\text{V}\cdot\text{Total}} \times Q^{\text{Mainen}}_{\bar{g}_\text{V}}$	1.61×10^{-2}	3.00×10^{-3}	$\times$	6.42×10^{-3}	$\frac{S}{cm^2}$
$\bar{g}^{\text{myelin0}}_{\text{K}_\text{V}}$	4.82×10^{-3}	$\times$	$\times$	$\times$	$\frac{S}{cm^2}$
$\bar{g}^{\text{myelin0}}_{\text{K}_\text{V}} \times Q^{\text{Mainen}}_{\bar{g}_\text{V}}$	4.82×10^{-3}	$\times$	$\times$	$\times$	$\frac{S}{cm^2}$
$R^{\text{myelin0}}_{\text{Passive}}$	1.12×10^{4}	4.00×10^{4}	3.00×10^{4}	3.00×10^{4}	$\Omega \cdot cm^2$
$g^{\text{myelin0}}_{\text{Passive}}$	8.94×10^{-5}	2.50×10^{-5}	3.33×10^{-5}	3.33×10^{-5}	$\frac{S}{cm^2}$
$g^{\text{myelin0}}_{\text{Cl}^-,\text{ leak}}$	1.34×10^{-5}	$\times$	$\times$	$\times$	$\frac{S}{cm^2}$
$g^{\text{myelin0}}_{\text{Na}^+,\text{ leak}}$	1.43×10^{-5}	$\times$	$\times$	$\times$	$\frac{S}{cm^2}$
$g^{\text{myelin0}}_{\text{K}^+,\text{ leak}}$	6.18×10^{-5}	$\times$	$\times$	$\times$	$\frac{S}{cm^2}$
$I^{\text{myelin0}}_{\text{MaxPump}}$	8.51×10^{-3}	$\times$	$\times$	$\times$	$\frac{mA}{cm^2}$
$V^{\text{myelin0}}_{\text{m}}$	-69.4	-70.0	-70.0	-70.0	mV
$E^{\text{myelin0}}_{\text{leak}}$	$\times$	-70.0	-70.0	-70.0	mV
$E^{\text{myelin0}}_{\text{Cl}}$	-70.0	$\times$	$\times$	$\times$	mV
$E^{\text{myelin0}}_{\text{Na}}$	60.0	60.0	50.0	60.0	mV
$E^{\text{myelin0}}_{\text{K}}$	-90.0	-90.0	-90.0	-90.0	mV

	$[\mathrm{Cl}^-]_{\mathrm{in}}^{\mathrm{myelin0}}$	11.0	×	×	×	mM
	$[\mathrm{Cl}^-]_{\mathrm{out}}^{\mathrm{myelin0}}$	151.0	×	×	×	mM
	$[\mathrm{Na}^+]_{\mathrm{in}}^{\mathrm{myelin0}}$	15.0	×	×	×	mM
	$[\mathrm{Na}^+]_{\mathrm{out}}^{\mathrm{myelin0}}$	141.6	×	×	×	mM
	$[\mathrm{K}^+]_{\mathrm{in}}^{\mathrm{myelin0}}$	140.0	×	×	×	mM
	$[\mathrm{K}^+]_{\mathrm{out}}^{\mathrm{myelin0}}$	4.8	×	×	×	mM
section	Parameter Name	OurModel	Mainen95	Mainen96	Hu2009	units
ranvier0						
	$\bar{g}_{\mathrm{Na_V}\cdot\mathrm{Total}}^{\mathrm{ranvier0}}$	8.03×10^{-1}	3.0	3.0	0.16	$\frac{S}{cm^2}$
	$\bar{g}_{\mathrm{Na_V}\cdot\mathrm{Total}}^{\mathrm{ranvier0}} \times Q_{\bar{g}_{\mathrm{V}}}^{\mathrm{Mainen}}$	8.03×10^{-1}	3.0	9.628	5.13×10^{-1}	$\frac{S}{cm^2}$
	$\bar{g}_{\mathrm{K_V}}^{\mathrm{ranvier0}}$	2.41×10^{-1}	×	×	×	$\frac{S}{cm^2}$
	$\bar{g}_{\mathrm{K_V}}^{\mathrm{ranvier0}} \times Q_{\bar{g}_{\mathrm{V}}}^{\mathrm{Mainen}}$	2.41×10^{-1}	×	×	×	$\frac{S}{cm^2}$
	$R_{\mathrm{Passive}}^{\mathrm{ranvier0}}$	2.24×10^{2}	5.00×10^{1}	5.00×10^{1}	5.00×10^{1}	$\Omega \cdot cm^2$
	$g_{\mathrm{Passive}}^{\mathrm{ranvier0}}$	4.47×10^{-3}	2.00×10^{-2}	2.00×10^{-2}	2.00×10^{-2}	$\frac{S}{cm^2}$

$g^{\text{ranvier0}}_{\text{Cl}^-,\text{ leak}}$	6.69×10^{-4}	×	×	×	$\frac{S}{cm^2}$
$g^{\text{ranvier0}}_{\text{Na}^+,\text{ leak}}$	7.13×10^{-4}	×	×	×	$\frac{S}{cm^2}$
$g^{\text{ranvier0}}_{\text{K}^+,\text{ leak}}$	3.09×10^{-3}	×	×	×	$\frac{S}{cm^2}$
$I^{\text{ranvier0}}_{\text{MaxPump}}$	4.26×10^{-1}	×	×	×	$\frac{mA}{cm^2}$
$V^{\text{ranvier0}}_{\text{m}}$	-69.4	-70.0	-70.0	-70.0	mV
$E^{\text{ranvier0}}_{\text{leak}}$	×	-70.0	-70.0	-70.0	mV
$E^{\text{ranvier0}}_{\text{Cl}}$	-70.0	×	×	×	mV
$E^{\text{ranvier0}}_{\text{Na}}$	60.0	60.0	50.0	60.0	mV
$E^{\text{ranvier0}}_{\text{K}}$	-90.0	-90.0	-90.0	-90.0	mV
$[\text{Cl}^-]^{\text{ranvier0}}_{\text{in}}$	11.0	×	×	×	mM
$[\text{Cl}^-]^{\text{ranvier0}}_{\text{out}}$	151.0	×	×	×	mM
$[\text{Na}^+]^{\text{ranvier0}}_{\text{in}}$	15.0	×	×	×	mM
$[\text{Na}^+]^{\text{ranvier0}}_{\text{out}}$	141.6	×	×	×	mM
$[\text{K}^+]^{\text{ranvier0}}_{\text{in}}$	140.0	×	×	×	mM
$[\text{K}^+]^{\text{ranvier0}}_{\text{out}}$	4.8	×	×	×	mM